buildings

MDPI

Article

A Study on the Preparation and Performance Optimization of Alkali-Activated Fly Ash-Based Aerogel-Modified Foam Concrete

Peng Liu [1,2], Wei Wu [2] and Yanfeng Gong [2,*]

[1] Jiangsu Collaborative Innovation Center for Building Energy Saving and Construction Technology, Jiangsu Vocational Institute of Architectural Technology, Xuzhou 221000, China; 761162899@qq.com
[2] College of Civil Engineering, Nanjing Tech University, Nanjing 211800, China; 1321824130@qq.com
* Correspondence: catherine19890107@163.com

Abstract

To address the energy and environmental challenges, this study targets the need for ultra-low energy buildings in China's hot summer-cold winter region (HSCW) by developing high-performance alkali-activated foam concrete (AAFC) insulation material. Initially, a target performance indicator system was established. Subsequently, a mix proportion design method based on the volume method was proposed, and preliminary mix proportions were designed and tested to achieve the target performance. Accordingly, eight factors, including alkali equivalent and SiO_2 aerogel content, were selected for further optimization. A systematic optimization of performance was then conducted using an $L_{32}(4^8)$ orthogonal experimental design. Range analysis and analysis of variance indicated that foam content significantly affected all target properties. The water-to-binder ratio notably influenced mechanical performance and dry density. Alkali equivalent and activator modulus directly regulated the reaction process. Notably, the incorporation of 2.5 wt% SiO_2 aerogel reduced the thermal conductivity to 0.1107 W/(m·K), highlighting its significant role in improving thermal insulation and effectively resolving the common trade-off between insulation and mechanical properties in FC. Furthermore, the waterproofing agent played a critical role in reducing water absorption and enhancing frost resistance. Finally, the optimal mix proportion was determined through matrix analysis, with all material properties meeting the expected targets. Test results confirmed that the optimized FC achieved a dry density of 576.34 kg/m^3, compressive and flexural strengths of 5.83 MPa and 1.41 MPa, respectively, a drying shrinkage rate of only 0.614 mm/m, a mass water absorption of 3.87%, and strength and mass loss rates below 10.5% and 1.8% after freeze–thaw cycles. Therefore, this material presents a novel solution for the envelope structures of low-energy buildings.

Keywords: FA; high-performance AAFC; SiO_2 aerogel; ultra-low energy consumption buildings; waterproofing

Check for updates

Academic Editor: Grzegorz Ludwik Golewski

Received: 20 November 2025
Revised: 24 December 2025
Accepted: 29 December 2025
Published: 2 January 2026

Copyright: © 2026 by the authors. Licensee MDPI, Basel, Switzerland. This article is an open access article distributed under the terms and conditions of the Creative Commons Attribution (CC BY) license.

1. Introduction

As smart cities emerge as a pivotal paradigm in global urban modernization, their integrated framework positions environmental sustainability as a central objective, driving urban transformation through systematic interventions in infrastructure, energy, and the environment [1]. Within this context, the building sector—a major consumer of resources and energy—faces urgent pressure to transition toward green and low-carbon development models. Projections suggest that buildings in China will account for more than 40% of total societal energy consumption by 2050 [2]. Supported by national policy directives, China's

construction industry is shifting toward an ultra-low energy consumption paradigm, heightening the need for high-performance, energy-efficient building materials. Foamed concrete (FC) is considered a promising material due to its thermal insulation, fire resistance, and low cost. However, conventional FC largely depends on ordinary Portland cement (OPC), a high-carbon binder that conflicts with sustainability goals. In contrast, alkali-activated materials offer a potentially lower-carbon alternative, with studies indicating up to an 80% reduction in carbon emissions compared to OPC [3,4]. Despite this advantage, AAFC still encounters challenges related to stability control, mix design optimization, and reaction mechanisms, which limit its large-scale application and underscore the need for further in-depth research.

The properties of AAFC are significantly influenced by the raw material composition, activator parameters, and production methods. Waste utilization strategies significantly enhance specific properties: FA with clinoptilolite improves thermal and frost resistance [5,6], pinecone powder increases the 91-day strength by 256.6% [7], recycled brick powder with Na_2O reduces thermal conductivity to 0.1067–0.1121 W/(m·K) [8,9], and waste glass enhances mechanical and corrosion resistance [10]. Process optimization through red mud addition and mechanical activation improves the pore structure and strength [11,12], while advanced composites containing hollow glass beads, rice husk, silica fume, and FA demonstrate synergistic thermal-mechanical performance enhancement [13–16]. A key limitation of strategies focusing on composite waste streams originates from the substantial source-to-source variation in their chemical composition and physical characteristics. This inherent inconsistency is directly translated into unpredictable performance, thereby constraining the development of universally applicable and scalable solutions for the building sector. Lightweight design strategies are implemented through the incorporation of Expanded Polystyrene (EPS) beads [17], waste polyurethane (PUR) [18], and lightweight aggregates [19], with densities of $\leq$800 kg/m^3 and thermal conductivity as low as 0.07 W/(m·K) being achieved. Foaming techniques, including chemical (H_2O_2 and zinc/aluminum metal powders) and physical methods (Sodium Dodecyl Sulfate(SDS)), allow tailored pore structures. The H_2O_2/SDS combination enables the production of materials with either ultra-low thermal conductivity (0.072 W/(m·K)) or high compressive strength (19.6 MPa) [20–22], demonstrating flexibility in property design through processing optimization. However, existing studies often focus on improving only one or a few specific properties (e.g., strength, thermal conductivity), placing excessive emphasis on single performance indicators while lacking in-depth investigation into the balance of multi-objective properties.

The pore characteristics critically govern the thermal and mechanical properties of AAFC. Jaya et al. [23] identified that the activator composition primarily controls the compressive strength (0.4–6 MPa), whereas the precursor/activator ratio dictates the thermal conductivity (0.11–0.30 W/(m·K)). The synergistic use of H_2O_2 and Tween 80 enabled porosity control within 36–86%. A more than two-fold increase in the 28-day strength was achieved by Su et al. [24] by optimizing the activator modulus (SiO_2/Na_2O = 1.2–1.8) under high-humidity curing conditions (RH $\geq$ 90%). A key research challenge is to balance low thermal conductivity with high strength. Huan et al. [25] developed a hierarchically porous material with 93.8% porosity and 0.040 W/(m·K) thermal conductivity, albeit at low strength (0.27 MPa). In contrast, Berkouche et al. [26] balanced both properties (0.13 W/(m·K), 4.26 MPa) using rice husk ash (RHA) and glass powder (GP). RHA enhanced the strength through geopolymerization, whereas GP refined the pore structure as an inert filler. The microstructural analysis confirmed that the performance stems from the synergy between the gel phases (C-A-S-H/N-A-S-H) and pore distribution. However, pore regulation cannot simultaneously optimize thermal and mechanical

properties, and its precise control and large-scale application remain difficult. Therefore, nanomaterials provide a superior approach for tailoring material properties. Rong et al. [27] demonstrated that combining 12% aerogel with 75% foam reduces thermal conductivity to 0.18 W/(m·K), while adding 1% polypropylene fibers increases compressive strength to 23.7 MPa. Similarly, Pan et al. [28] found that silica aerogel decreases the thermal conductivity by 24% (to 0.0886 W/(m·K)) through multi-scale porosity, and Ji et al. [29] reported that 0.4% CMC enhances the pore structure, improving the strength by 44.7% and pore sphericity.

Based on the aforementioned limitations, this study addresses the following research question: How can we, through material design and process control, develop a novel low-carbon building material system that moves beyond the limitations of single-performance optimization? This involves establishing a multi-objective synergistic design strategy to co-optimize thermal and mechanical properties, overcoming the inherent conflict between pore structure control and engineering feasibility, and ensuring scalability. The ultimate goal is to provide a sustainable material solution for ultra-low-energy buildings.

This study is systematically structured into five parts from the perspectives of methodology and theoretical foundation [1,30]. First, the introduction provides an overview of the current state of research, identifies existing gaps, and establishes the research objectives. This study is oriented toward practical engineering applications. AAFC was developed by employing alkali activation technology using FA as the sole aluminosilicate solid raw material. The research focuses on the co-optimization of multiple properties to meet the comprehensive performance requirements of ultra-low-energy building envelopes, particularly for construction in the HSCW. Second, a comprehensive set of seven key performance indicators was established, including thermal conductivity, mechanical strength, fire resistance, and freeze–thaw durability. Notably, critical emphasis was placed on enhancing waterproofing performance, effectively addressing the long-standing issue of high water absorption in conventional FC. Subsequently, a combined approach of orthogonal experimental design and matrix analysis was adopted to achieve the desired performance optimization. Specifically, SiO_2 aerogel—a super thermal insulation material—was incorporated to improve the thermal performance of AAFC. This strategy resolves the inherent conflict between the mechanical and thermal properties observed in conventional FC. Ultimately, all tested parameters satisfied the requirements of the established performance index system, resulting in a synergistic enhancement across the range of key material properties.

2. Construction of Target Performance Index System for AAFC

2.1. Determination of Target Performance Indicators and Parameters

To meet the energy efficiency demands of ultra-low-energy buildings in the HSCW. A high-performance AAFC has been developed. It achieves self-insulation in 300 mm-thick exterior walls while meeting mechanical standards for non-load-bearing structures. The material also exhibits excellent water resistance. Furthermore, it conforms to specifications for dry density, fire resistance, and frost resistance.

(1) Dry Density and Mechanical Properties

The dry density was optimized by balancing the sound insulation and the mechanical requirements. For non-load-bearing exterior walls, mechanical targets–compressive strength, flexural strength, and drying shrinkage were defined according to relevant standards [31–33].

(2) Thermal Performance

The thermal performance was characterized by two key parameters: wall thermal transmittance and thermal conductivity of the AAFC. To fulfill the self-insulation crite-

ria for ultra-low energy buildings in the HSCW, the thermal transmittance was limited to ≤0.4 W/(m^2·K) [34–36]. The exterior wall thickness is set to 300 mm. The thermal conductivity of the AAFC was then calculated in compliance with the relevant design codes, as follows [37]:

$$K = 1/\left(\frac{1}{h_1} + \frac{1}{h_2} + \frac{\delta}{\lambda}\right) \quad (1)$$

In the equation, K(0.4 W/(m^2·K)) is the wall thermal transmittance; h_1 and h_2 are the interior and exterior surface heat transfer coefficients, taken as 8.7 and 23 W/(m^2·K, respectively, with the latter representing the most severe condition; δ is the wall thickness (0.3 m); λ is the thermal conductivity of the AAFC(W/(m·K)); and a thermal conductivity correction factor (α) of 1.05 was incorporated. Thus, the corresponding thermal conductivity of AAFC should not exceed 0.1216 W/(m·K).

(3) Fire Resistance and Water Resistance

The AAFC material exhibits Class A fire resistance as an inorganic noncombustible material, thus meeting these requirements.

To address the inherent drawback of high water absorption in FC, mass water absorption was adopted as a key performance indicator. The influence of moisture content (varied from 0% to 55% at 5% intervals) on the thermal conductivity was investigated using the weight method. A well-fitted correlation (R^2 = 0.97669) was established between the thermal conductivity and water absorption, demonstrating a significant dependence of thermal performance on moisture content.

$$\lambda = 0.2016 + 0.00853x - 0.0001x^2 \quad (2)$$

where λ is the thermal conductivity of the AAFC(W/(m·K)); x is the mass water absorption (%); the results are shown in the figure below:

The thermal conductivity was observed to increase by 105.31% with rising moisture content. The value rose from 0.1975 W/(m·K) when dry to 0.4055 W/(m·K) at 55% moisture content, as shown in Figure 1. A near-linear rapid rise occurred within 0–10% absorption, where the conductivity exceeded the target value by 37.35%. Given that the existing standards are inadequate for practical requirements [31], the mass water absorption is targeted at ≤5% based on a comprehensive analysis.

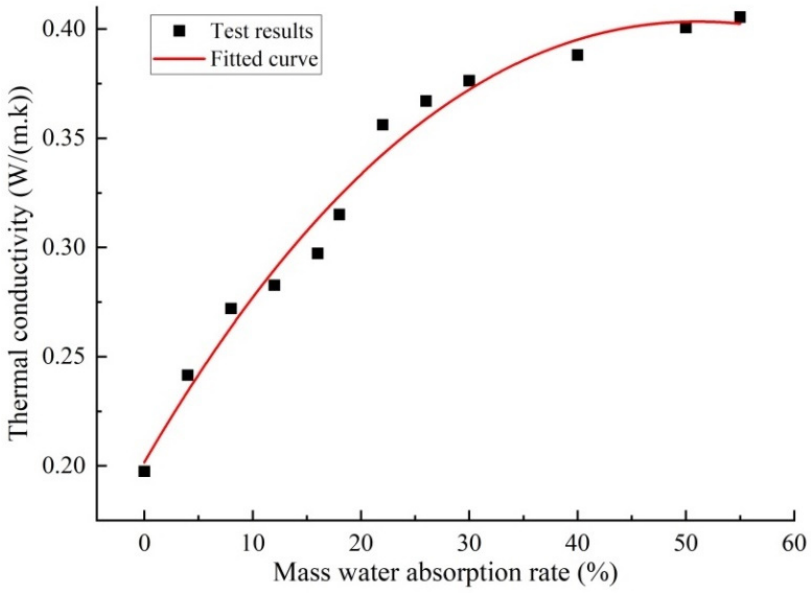


Figure 1. Fitting curve of thermal conductivity with mass water absorption rate.

(4) Frost Resistance

According to the Chinese National Standard, the frost resistance for the HSCW is set as F25 [33], with the strength and mass loss rates serving as the secondary indicators.

2.2. Target Performance Indexes of AAFC

According to the requirements in Section 2.1, the target performance indices established and the corresponding values are presented in Table 1 below.

Table 1. Target performance indexes.

First-Level Indicator Type	Second-Level Indicator Name	Target Value
Bulk Density	Dry Density ρ	A06 ($\leq$650 kg/m^3)
Thermal Performance	Thermal Transmittance K Thermal Conductivity λ	Wall Thickness 300 mm, $\leq$0.4 W/m^2·K $\leq$0.1216 W/(m·K)
Fire Resistance	Combustion Performance Rating F_{RL}	Class A (Non-Combustible Material)
Water Resistance	Mass Water Absorption Wr	$\leq$5%
Mechanical Properties	Compressive Strength f Flexural Strength R_f	$\geq$5 MPa $\geq$1.0 Mpa
	Drying Shrinkage ε	$\leq$1 mm/m
Frost Resistance (F25)	Strength Loss Rate F_c Mass Loss Rate M_m	$\leq$25% $\leq$5%

3. Mix Proportion Design Method for AAFC and Testing Protocol

3.1. Basic Principles

A mix proportion design method for the AAFC was developed based on the volumetric method. The underlying principle is defined as the volume of the fresh slurry being equal to the sum of the volumes of all solid components and the entrapped air. The design process follows three steps: target performance values are first established; theoretical dosages of raw materials are then calculated; and finally, the mix proportion is refined through experimental adjustments. The dry density was selected as the primary design target because of its ease of control.

3.2. Design Steps and Calculation Methods for Mix Proportion

Based on the above principles, the mix proportion design steps for the AAFC are as follows:

(1) The mass of each precursor component and other curable materials was determined according to the target dry density of the AAFC.

(2) Determine the water-to-binder ratio, activator dosage, and additional water amount, based on the precursor dosage.

(3) The volume of each constituent material in the slurry was calculated to determine the foam volume.

(4) The foam mass was determined using the calculated foam volume and foam density.

(5) The required foaming agent mass was calculated based on its dilution ratio and foam mass.

The mix proportion design relationship for the precursor (including silico-aluminate raw materials)–activator–physical foaming system is as follows:

$$\rho_d = \left(m_{pre} + m_{act} + \sum_{i=1}^{n} m_i \right) \times S_a \quad (3)$$

where ρ_d denotes the design dry density of the AAFC (kg/m^3); m_{pre} represents the mass of precursor materials in 1 m^3 of AAFC (kg); m_{act} is the mass of the curable portion of the alkali activator in 1 m^3 of AAFC (kg); and m_i denotes the mass of each additional curable raw material in 1 m^3 of AAFC (kg). The mass coefficient Sa is given by the ratio of total dry mass to cured non-evaporable matter mass. Its experimentally determined values range from 1.0 to 1.3.

In the preparation of 1 m^3 AAFC slurry, the sum of the volumes of silico-aluminate-containing precursor materials, activator, water required except for diluting the foaming agent, and other curable raw materials is denoted as V_1, which is calculated using Equation (4); the portion where the slurry volume is less than 1 m^3 is considered to be filled by foam, and the foam volume V_2 can be calculated using Equation (5).

$$V_1 = \frac{m_{pre}}{\rho_{pre}} + \frac{m_{act}}{\rho_{act}} + \frac{m_w}{\rho_w} + \sum_{i=1}^{n} m_i / \sum_{i=1}^{n} \rho_i \quad (4)$$

where V_1 denotes the sum of the volumes of precursor materials, activator, water required except for diluting the foaming agent, and other curable raw materials (m^3); m_w represents the mass of water required except for diluting the foaming agent (kg); ρ_{pre} is the density of the precursor materials (kg/m^3); ρ_{act} is the density of the prepared activator (kg/m^3); ρ_w is the density of water (kg/m^3), with a value of 1000 kg/m^3; and ρ_i denotes the respective densities of other curable raw materials in the AAFC (kg/m^3).

$$V_2 = k\,(1 - V_1) \quad (5)$$

where V_2 denotes the foam content in 1 m^3 of AAFC (m^3/m^3); k is the surplus coefficient, which should be determined according to the type and quality of the foaming agent, foam preparation time, etc., for foaming agents with good stability; the value range is 1.1 to 1.4; and the specific value is determined through experimental and theoretical analysis.

The dosage of the foaming agent m_f in 1 m^3 of AAFC can be calculated using Equations (6) and (7):

$$m_p = V_2 \times \rho_{foam} \quad (6)$$

where m_p denotes the mass of foam in 1 m^3 of AAFC (kg), and ρ_{foam} denotes the mass of foam in 1 m^3 of FC (kg).

$$m_f = m_p \div (\beta + 1) \quad (7)$$

where m_f denotes the dosage of foaming agent in 1 m^3 of AAFC (kg), and β represents the dilution multiple of the foaming agent, which can be determined through experiments.

3.3. Testing Protocol and Test Raw Materials

3.3.1. Testing Protocol

(1) Major Experimental Instruments

The main instruments and their specifications used in the experiments are listed in Table 2 below.

Table 2. Major experimental instruments and specifications.

Name	Model and Key Specifications	Name	Model and Key Specifications
X-ray fluorescence spectrometry (XRF)	Thermo Scientific ARL 9900 X-ray Workstation, Thermo Fisher Scientific Inc., Ecublens, Switzerland.	Analytical Balance	LICHEN JII 2012,Shanghai Lichen Instrument Technology Co., Ltd., Shanghai, China. Weighing Capacity: 0~2100 g Readability: 0.001 g
X-ray diffraction (XRD)	Ultima IV X-ray Diffractometer, Rigaku Corporation, Tokyo, Japan. Diffraction angle 2θ:10~80°	Thermal Conductivity Analyzer (Hot Disk)	DRE-III, Hunan Xiangtan Xiangyi Instrument Co., Ltd.; Xiangtan, China. Measurement range: 0.01~500 W/(m·K) Resolution: 0.0001 W/(m·K)
SEM/SEM-EDS	JSM-IT500HR Scanning Electron Microscope, JEOL Ltd., Tokyo, Japan.	Universal Compression-Flexure Testing Machine	EUT3305-C, Jinan Sanqin Testing Technology Co., Ltd., Jinan, China. Maximum Compressive Test Force: 300 kN Maximum Flexural Test Force: 10 kN
Electric thermostatic blower drying oven	ShuLi FX101-1, Shanghai Shuli Instrument and Meter Co., Ltd., Shanghai, China. Temperature Range: Room Temperature to 250 °C, Sensitivity: ±1 °C	Low-Temperature Freezer	Guoli GDW-050,Changzhou Guoli Testing Equipment Research Institute, Changzhou, China. Minimum Temperature: −60 °C Accuracy: ≤ ±0.5 °C

(2) Test Methods

For AAFC, the tests of dry density, thermal conductivity, water absorption by mass, compressive strength, and frost resistance were carried out using 100 mm cube specimens. Flexural strength and drying shrinkage tests were performed using 40 mm × 40 mm × 160 mm prism specimens. Three parallel specimens were prepared for each test group. All specimens were dried to constant mass prior to testing. The experiments were conducted using the instruments listed in Table 2, in strict accordance with the relevant testing standards. The arithmetic mean of three measurements was taken as the result for each performance indicator to ensure data accuracy.

3.3.2. Test Raw Materials

(1) FA and activators

FA from China Resources Power(Xuzhou) Co., Ltd., Xuzhou, China was used as the primary raw material. The XRF analysis of the FA (Table 3) indicates that its main components are SiO_2 and Al_2O_3. The total content of SiO_2, Al_2O_3, and Fe_2O_3 exceeds 70%. The CaO content is 3.34% (<10%), which classifies it as Class F low-calcium FA. The XRD pattern (Figure 2) exhibits a distinct broad hump and multiple long-range fluctuations, confirming a high amorphous content. This amorphous phase is the primary source of its pozzolanic activity. Sharp diffraction peaks correspond to crystalline phases such as quartz, mullite, free CaO, $CaSO_4$, and hematite.

Table 3. Chemical compositions of FA (wt%).

SiO_2	Al_2O_3	Fe_2O_3	CaO	SO_3	TiO_2	K_2O	Other Components	Moisture Content	LOSS
49.92	31.98	3.76	3.34	1.10	1.26	1.43	7.21	0.07	4.63

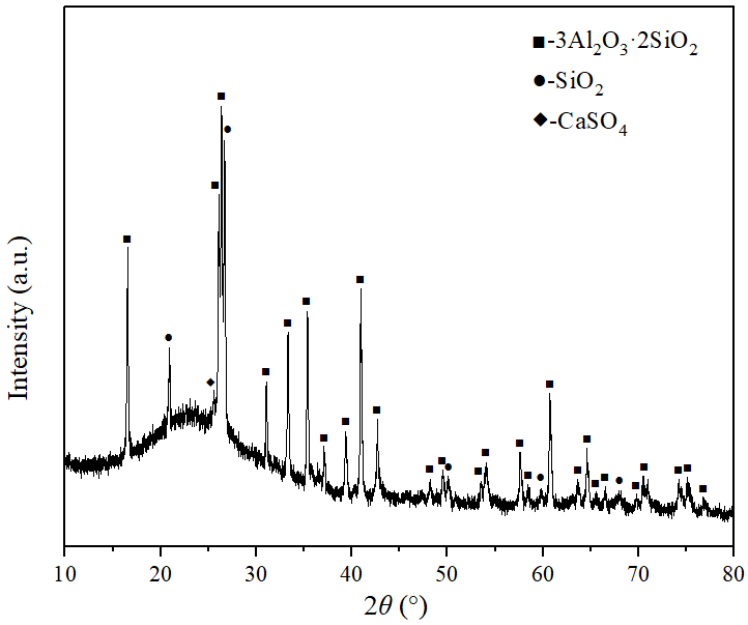


Figure 2. XRD patterns of FA.

As shown in Figure 3a, the FA exhibits an ultra-fine particle size distribution, with a D50 of 7.734 μm, a mean particle size of 9.196 μm, and a specific surface area of 1.416 m^2/g. These characteristics contribute to enhanced pozzolanic activity and improved cement matrix strength development. SEM analysis (Figure 3b,c) reveals that the FA consists of spherical particles with smooth surfaces (cenospheres and plerospheres) along with irregular particles (such as quartz and mullite).

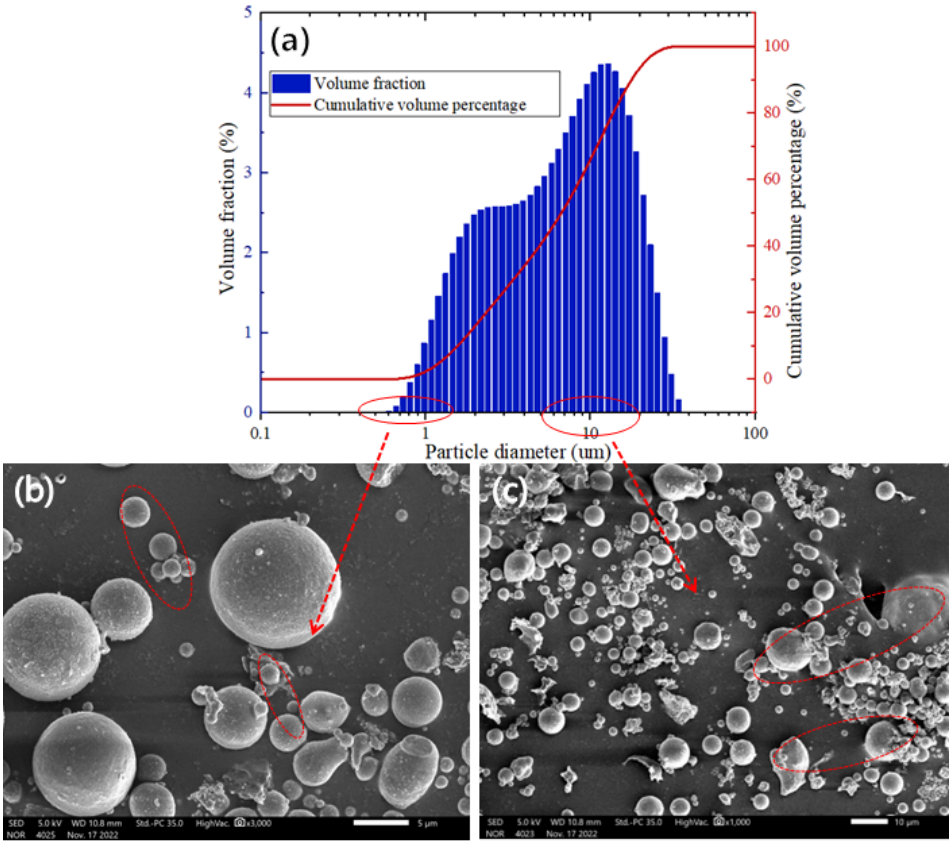


Figure 3. Particle characteristics and micromorphology of FA, (**a**) particle size distribution, (**b**,**c**) micromorphology of FA (SEM).

A binary composite activator was prepared by mixing water glass (modulus = 3.3, Baume degree = 38.5°Be′) from Yourui Refractory Materials Co., Ltd., Jiashan, China with sodium hydroxide (NaOH, ≥99% purity, IS-I grade) supplied by Shandong Binzhou Chemical Group Co., Ltd., Binzhou, China. The composite activator was prepared as follows. Sodium hydroxide (NaOH) was first weighed according to the target modulus, followed by dissolution in deionized water. The resulting solution was allowed to cool to room temperature before being thoroughly mixed with sodium silicate (water glass). The final mixture was then homogenized and stored in a sealed container for subsequent use.

(2) Foaming Agents

The HTQ-1 composite polymer foaming agent was supplied by Henan Huatai New Material Technology Co. Ltd., Nanyang, China. The foaming agent is diluted with water at a mass ratio of 1:40 (w/w). Its performance was tested in accordance with the national standards [38] under a foaming pressure of 0.5 MPa. The foaming performance parameters are listed in Table 4.

Table 4. Performance parameters of foaming agent.

Project	Foaming Agent Multiple (n)	Foaming Density (kg/m^3)	1 h Sedimentation Distance (mm)		Sedimentation Distance (cm/h)	
			First-Class Product	Qualified Product	First-Class product	Qualified Product
Indicator	15~30	— —	≤50	≤70	≤70	≤80
Test Results	28	62.1	41.1		59.6	

(3) Lightweight Aggregate—Vitrified Microspheres

Lightweight aggregates can reduce density while enhancing mechanical properties. Vitrified microspheres (Figure 4a) from Hebei Yixin Energy Conservation and Thermal Insulation Building Materials Co., Ltd., Hengshui, China were used. The properties are listed in Table 5.



Figure 4. Raw materials: (**a**) vitrified microbeads, (**b**) basalt fiber, (**c**) HPMC, (**d**) calcium hydroxide, (**e**) sodium methylsilicate solution.

Table 5. Performance parameters of vitrified microbeads.

Particle Size (mm)	Bulk Density ($kg/m^{3)}$	Cylinder Pressure Strength (MPa)	Thermal Conductivity (W/(m·K))	Water Absorption Rate (%)	Floating Rate (%)	Surface Vitrification Closed-Cell Rate (%)	Linear Shrinkage Rate (%)
1~3	116	0.52	0.049	30	≥80	≥80	0.29

(4) Basalt Fiber

The fibers enhanced the tensile strength of the FC. Basalt fibers (Figure 4b) from Changsha Ningxiang Building Materials Co., Ltd., Changsha, China were used, and their properties are listed in Table 6.

Table 6. Performance parameters of basalt fibers.

Fiber Length mm	Relative Density g/cm^3	Diameter μm	Elastic Modulus GPa	Tensile Strength MPa	Ultimate Elongation %
6	2.65	17	7.6	1050	3

(5) Foam Stabilizers.

Hydroxypropyl methylcellulose ether (HPMC) was used as the foam stabilizer. A white powder (Figure 4c) with a molecular weight of 86,000 and a viscosity of 200,000 effectively thickens the foam film and reduces defoaming or bubble merging.

(6) Calcium Hydroxide

Low-calcium FA served as the sole solid aluminosilicate source. Calcium hydroxide provided by Nanjing Baore Chemical Co., Ltd., Nanjing, China, morphology shown in Figure 4d, was introduced into the system to optimize the alkali-activation process and improve the compressive strength of the AAFC.

(7) Waterproofing Agents.

The internally admixed waterproofing agent sodium methyl silicate solution, as shown in Figure 4e, was produced by Shanxi Jing Chen Building Materials Co., Ltd., Yuncheng, China.

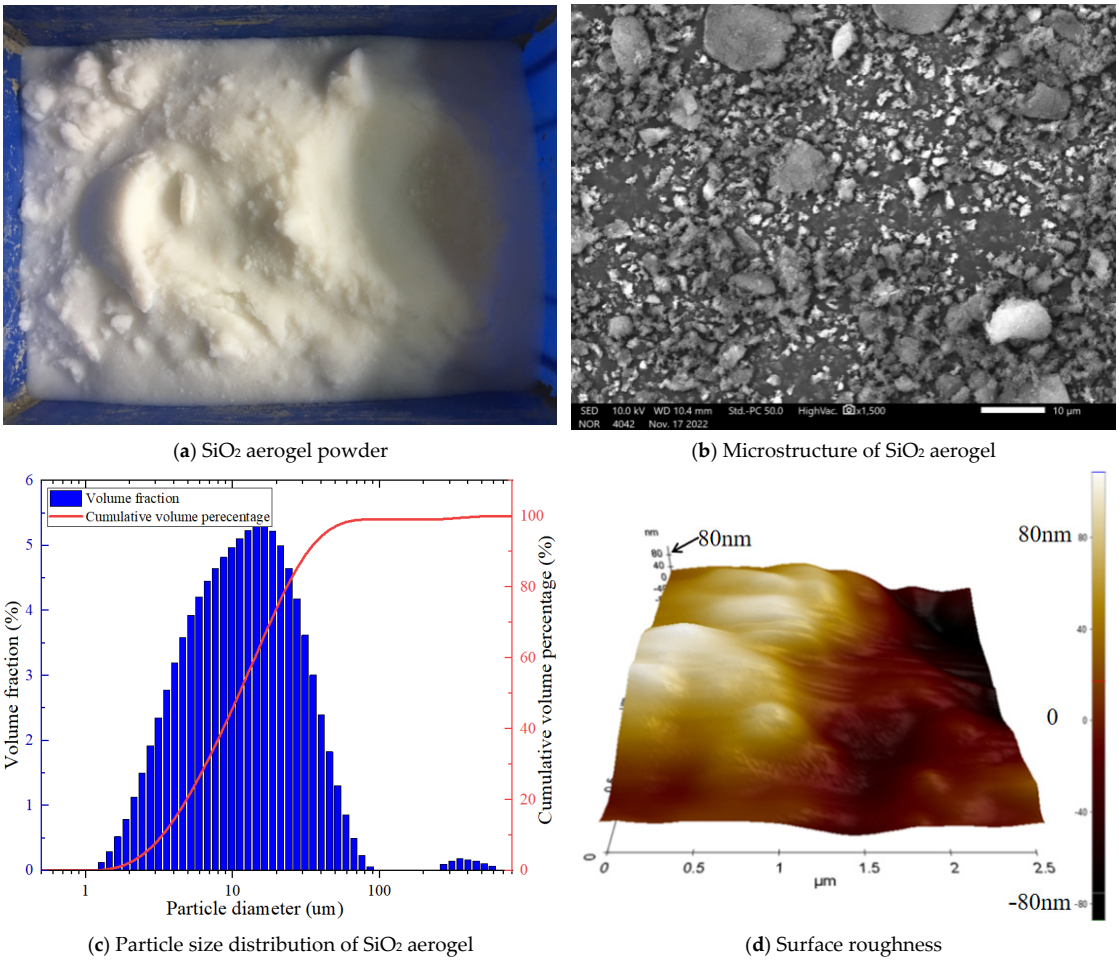
(8) SiO_2 Aerogel

The SiO_2 aerogel was supplied by Shenzhen Zhongning Technology Co., Ltd., Shenzhen, China and its performance parameters are summarized in Table 7 below.

Table 7. Performance parameters of silica aerogel powder.

Particle Size μm	Bulk Density kg/m^3	Pore Diameter nm	Porosity %	Specific Surface Area m^2/g	Thermal Conductivity W/(m·K)	Surface Properties
15~50	40~60	20~50	>90	500~800	<0.013	Hydrophobic

The SiO_2 aerogel appears as a white powder (Figure 5a) with an irregular particle morphology and a broad size distribution ranging from 3.78 to 37.1 μm (D90 = 37.1 μm), as shown in Figure 5b,c. Its high specific surface area (707.8 m^2/kg) and nanoscale surface roughness (amplitude ≈ 80 nm, Figure 5d) contribute to its effective thermal insulation, which stems from its nanoporous structure that markedly suppresses both solid conduction and gas convection [27,28].



(**a**) SiO_2 aerogel powder (**b**) Microstructure of SiO_2 aerogel

(**c**) Particle size distribution of SiO_2 aerogel (**d**) Surface roughness

Figure 5. Silica aerogel powder and its microscopic characteristics.

3.4. Experimental Verification of Mix Proportion Design Method and Preliminary Mix Design

A preliminary mix design was conducted using the proposed method based on the upper dry density limit (650 kg/m^3). For 1 m^3 AAFC, raw material dosages were calculated: foam from 40 times diluted foaming agent, alkali equivalent 0.1, empirical water-to-binder ratio 0.4, activator modulus 1.5. The raw materials are added in the order of solids first, followed by liquids. A planetary mixer was used to mix the ingredients at a speed of 200 r/min for no less than 2 min until a homogeneous mixture was achieved. The prepared slurry was then poured into standard molds for shaping. The cast specimens were cured at a room temperature of 25 °C for 48 h before demolding. Subsequently, they were further cured for 7 days in an environment maintained at 55 °C and 95% relative humidity. The specimens were sealed with PE film throughout the entire curing process. The calculation results are listed in Table 8 below.

Table 8. Raw material consumption for the initial mix.

FA (kg/m^3)	Sodium Silicate (kg/m^3)	Sodium Hydroxide (kg/m^3)	Foam Dosage (m^3/m^3)	Water-to-Binder Ratio	Additional Water Dosage (kg/m^3)
396.73	213.45	27.689	0.646	0.4	21.04

3.5. Testing and Results Analysis

The specimens were prepared according to the mix proportion and preparation process, and their relevant properties were tested. The test results are listed in Table 9.

Table 9. Test results of sample performance.

Dry Density	Thermal Conductivity	Mass Water Absorption Rate	Mechanical Properties			Frost Resistance (F25)	
ρ (kg/m^3)	λ (W/(m·K))	Wr (%)	f (MPa)	R_f (MPa)	ε (mm/m)	Fc (%)	M_m (%)
632.5	0.1975	57.1%	3.76	0.823	1.432	44.53%	17.36%

The preliminary mix specimens exhibit deficiencies in several key properties. The compressive strength (3.86 MPa), flexural strength (0.83 MPa), and drying shrinkage (1.432 mm/m) (Figure 6) fall short of their target values by 24.8% and 17.7%, respectively, and exceed their target values by 43.2%. The thermal conductivity reaches 0.1975 W/(m·K), exceeding the limit by 62.4%, while the mass water absorption (57.1%) is 11.42 times the target value. Poor water resistance also leads to excessive frost-induced damage, with the strength and mass loss rates surpassing their thresholds by 122.7% and 247.2%, respectively (Figure 7). Consequently, among all the properties evaluated, the feasibility of the design method is validated, but only the dry density meets the target requirements, indicating the necessity for comprehensive formulation optimization.

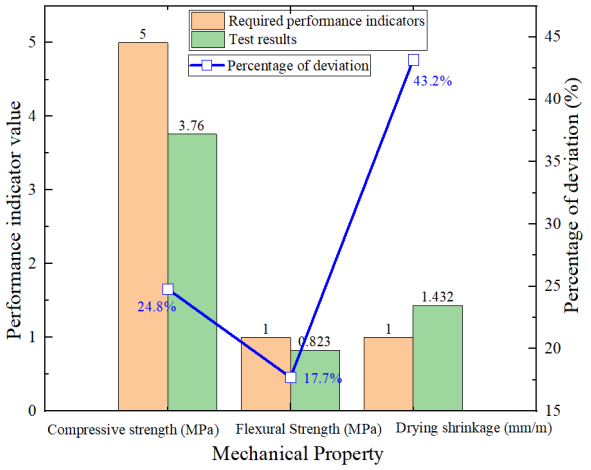


Figure 6. Test results of the mechanical properties of preliminary mix ratio samples and deviation rates from the target values.

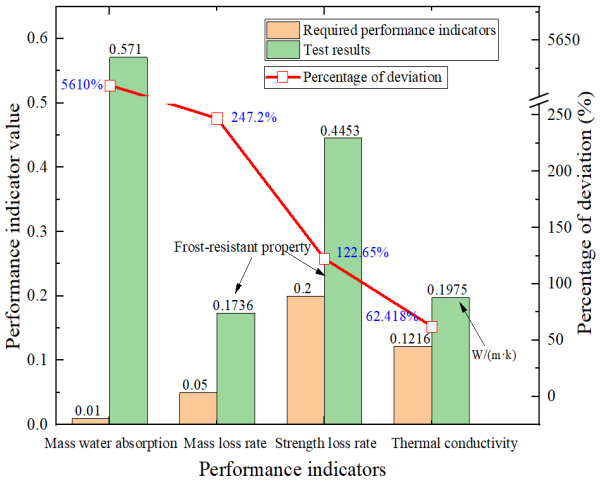


Figure 7. Test results of frost resistance and thermal conductivity of the preliminary mix ratio samples and deviation rates from the target values.

4. Performance Optimization of AAFC Based on Orthogonal Experimental Design

4.1. Performance Optimization Methods and Schemes

Based on the Preliminary Mix, an L_{32} (4^8) orthogonal experiment was designed for comprehensive performance optimization. Eight variables were set at four levels (Table 10). Considering foam loss, the foam volume dosage was 3.0–4.5 times the theoretical value. The foam stabilizer was added at 1–3.5% of the foaming agent mass. The SiO_2 aerogel content was 2–8 kg/m^3, while the dosages of the internal waterproofing agent and calcium hydroxide were based on the FA mass. The vitrified microspheres, basalt fiber, and curing process used fixed parameters of 5% and 1% of the FA mass for vitrified microspheres and basalt fiber, respectively.

Table 10. Levels of factors.

Level	Factors							
	Alkali Equivalent (A)	Activator Modulus (B)	Water-to-Binder Ratio (C)	Foam Dosage (D)	Foam Stabilizer Dosage (E)	Aerogel Dosage (F)	Calcium Hydroxide Dosage (G)	Waterproofing Agent Dosage (H)
1	0.08	0.9	0.40	3.0	1%	2	5%	1.5%
2	0.09	1.1	0.45	3.5	1.5%	4	10%	3%
3	0.10	1.3	0.55	4.0	2.5%	6	15%	4.5%
4	0.11	1.5	0.60	4.5	3.5%	8	20%	5.5%

4.2. Orthogonal Experimental Design

An orthogonal experimental design was constructed using the eight variables mentioned above, each at four levels. The factor-level table and orthogonal array are provided below:

Specimens were prepared according to the mix proportions listed in Table 11. The preparation and testing processes are shown in the Figure 8 below, and the performance test results for the specimens are listed in Table 12.

Table 11. Orthogonal experimental design table for L_{32} (4^8).

NO.	Factors								
	Alkali Equivalent (A)	Activator Modulus (B)	Water-to-Binder Ratio (C)	Foam Dosage (D)	Foam Stabilizer Dosage (E)	Aerogel Dosage (F)	Calcium Hydroxide Dosage (G)	Waterproofing Agent Dosage (H)	Empty Column (J)
1	1 (0.08)	1 (0.9)	1 (0.40)	1 (3.0)	1 (1%)	1 (2)	1 (5%)	1 (1.5%)	1
2	1	1	2 (0.45)	2 (3.5)	4 (3.5%)	4 (8)	3 (15%)	3 (4.5%)	2
3	1	2 (1.1)	3 (0.55)	4 (4.5)	1	2 (4)	3	4 (5.5%)	3
4	1	2	4 (0.60)	3 (4.0)	4	3 (6)	1	2 (3%)	4
5	1	3 (1.3)	1	3	2 (1.5%)	4	2 (10%)	4	4
6	1	3	2	4	3 (2.5%)	1	4 (20%)	2	3
7	1	4 (1.5)	3	2	2	3	4	1	2
8	1	4	4	1	3	2	2	3	1
9	2 (0.09)	1	3	4	3	4	2	1	4
10	2	1	4	3	2	1	4	3	3
11	2	2	1	1	3	3	4	4	2

Table 11. *Cont.*

NO.	Factors								
	Alkali Equivalent (A)	Activator Modulus (B)	Water-to-Binder Ratio (C)	Foam Dosage (D)	Foam Stabilizer Dosage (E)	Aerogel Dosage (F)	Calcium Hydroxide Dosage (G)	Waterproofing Agent Dosage (H)	Empty Column (J)
12	2	2	2	2	2	2	2	2	1
13	2	3	3	2	4	1	1	4	1
14	2	3	4	1	1	4	3	2	2
15	2	4	1	3	4	2	3	1	3
16	2	4	2	4	1	3	1	3	4
17	3 (0.10)	1	3	1	4	2	4	2	3
18	3	1	4	2	1	3	2	4	4
19	3	2	1	4	4	1	2	3	1
20	3	2	2	3	1	4	4	1	2
21	3	3	3	3	3	3	3	3	2
22	3	3	4	4	2	2	1	1	1
23	3	4	1	2	3	4	1	2	4
24	3	4	2	1	2	1	3	4	3
25	4 (0.11)	1	1	4	2	3	3	2	2
26	4	1	2	3	3	2	1	4	1
27	4	2	3	1	2	4	1	3	4
28	4	2	4	2	3	1	3	1	3
29	4	3	1	2	1	2	4	3	3
30	4	3	2	1	4	3	2	1	4
31	4	4	3	3	1	1	2	2	1
32	4	4	4	4	4	4	4	4	2

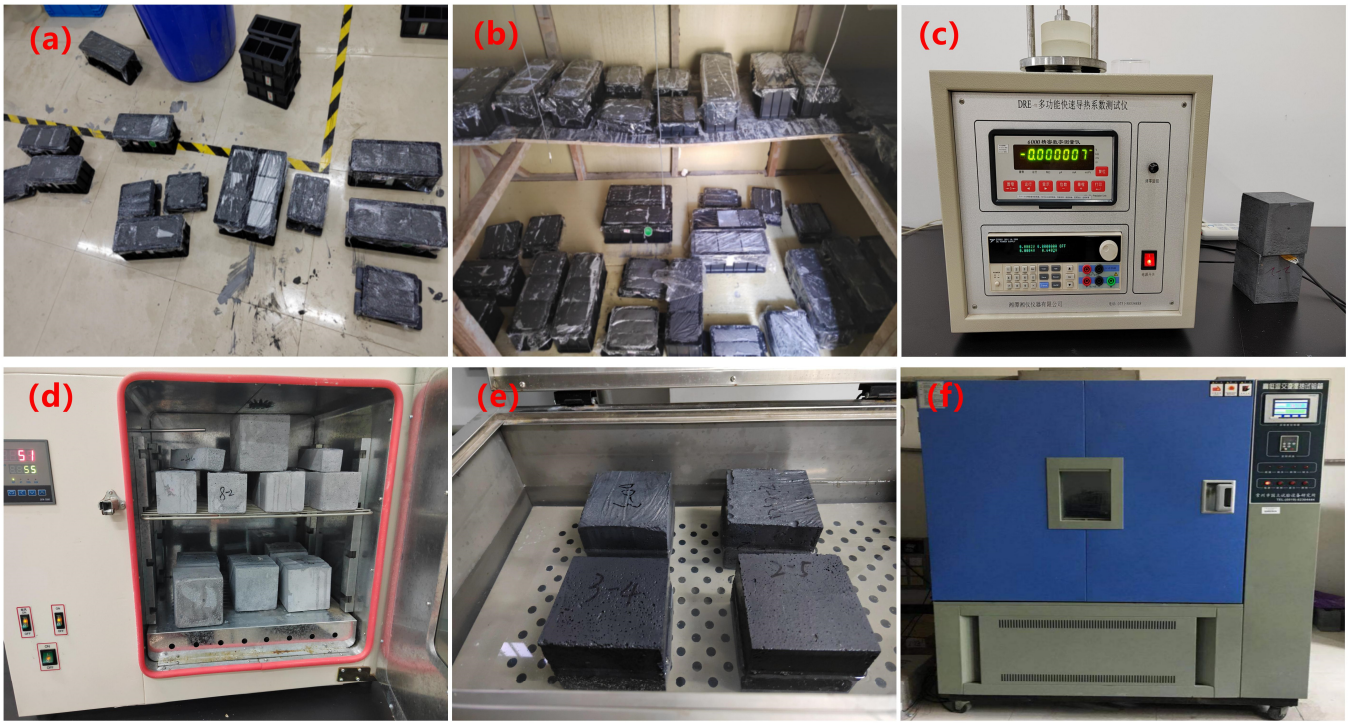


Figure 8. Samples preparation and testing, (**a**) samples preparation, (**b**) curing, (**c**) thermal conductivity measurement, (**d**) samples drying, (**e**) water absorption test, (**f**) frost resistance test.

Table 12. Performance test results of the mix ratio samples in the orthogonal test.

Index	Bulk Density	Thermal Performance	Water Resistance	Mechanical Properties			Frost Resistance (F25)	
NO.	ρ kg/m^3	λ W/(m·K)	Wr %	f MPa	R_f MPa	ε mm/m	F_c %	M_m %
1	654.82	0.1377	6.50	6.12	1.77	0.849	12.136	2.028
2	633.58	0.0990	4.41	5.47	1.21	0.841	11.124	1.623
3	568.23	0.1001	4.55	5.55	1.32	0.653	11.087	1.597
4	568.34	0.0994	5.50	5.23	1.01	0.747	12.391	2.016
5	581.37	0.0977	4.51	5.47	1.24	0.657	10.553	1.403
6	587.38	0.1138	5.74	5.62	1.38	0.623	12.245	1.981
7	592.23	0.1011	7.21	5.48	1.26	0.841	12.743	2.117
8	588.58	0.0996	4.46	5.31	1.11	0.933	11.135	1.701
9	563.62	0.0980	7.39	5.34	1.15	0.641	13.112	2.243
10	578.95	0.1137	4.69	5.58	1.37	0.738	11.653	1.781
11	655.77	0.1015	4.41	5.62	1.39	0.873	10.127	1.283
12	624.32	0.1022	5.33	6.11	1.85	0.822	11.753	1.887
13	618.79	0.1274	4.61	5.56	1.36	0.847	11.213	1.581
14	580.13	0.0968	5.55	5.64	1.42	1.025	11.873	1.904
15	588.27	0.1002	6.89	5.68	1.44	0.621	12.032	2.104
16	568.57	0.0990	4.81	5.4	1.15	0.608	11.038	1.647
17	621.65	0.1023	5.11	5.55	1.34	0.929	11.214	1.724
18	586.41	0.0988	4.64	5.46	1.18	0.841	10.876	1.549
19	579.69	0.1111	4.86	5.72	1.47	0.537	11.239	1.673
20	577.63	0.0970	4.77	5.24	1.08	0.718	13.037	2.221
21	574.29	0.1012	4.66	5.46	1.20	0.703	11.214	1.732
22	556.83	0.1028	7.41	5.33	1.14	0.704	13.463	2.362
23	643.22	0.0994	4.94	5.78	1.68	0.715	11.463	1.734
24	638.27	0.1304	4.49	6.03	1.78	0.903	10.357	1.352
25	578.61	0.0992	5.77	5.26	1.11	0.554	12.154	2.032
26	581.34	0.0999	4.45	5.47	1.21	0.694	10.443	1.427
27	604.32	0.0954	4.50	5.66	1.44	0.918	11.154	1.683
28	587.73	0.1102	6.55	5.78	1.49	0.835	12.522	2.124
29	645.38	0.1042	4.57	5.72	1.72	0.803	11.223	1.645
30	625.36	0.1008	4.41	5.77	1.52	0.922	12.231	2.102
31	585.66	0.1228	5.70	5.53	1.29	0.724	12.576	2.133
32	564.28	0.0929	4.52	5.27	1.11	0.687	11.137	1.644

As presented in the table above, the 32 mix proportion samples exhibit dry densities of 556.83–655.77 kg/m^3, with only two slightly exceeding the target. The thermal conductivity ranges from a minimum of 0.0929 W/(m·K) (sample 32) to a maximum of 0.1377 W/(m·K) (sample 1); only samples 1, 13, and 31 marginally exceed the target. The mechanical properties and freeze–thaw resistance (F25) meet these requirements. The lowest mass of water absorption is 4.12% (below the target), although 13 samples exceed the target. Further analysis is required to identify the optimal mix for achieving the best comprehensive performance.

4.3. Analysis of Influences of Different Factors on Performance

4.3.1. Range Analysis of Test Results

(1) Range Analysis of Dry Density

The range (R) values (Table 13) reveal that the foam content and water–binder ratio are the primary factors influencing dry density, with curves showing the steepest slopes (Figure 9). This trend is further confirmed by the variations in microscopic pore size

observed in the SEM results. In contrast, the aerogel content and calcium hydroxide content are secondary factors, while the remaining factors have minimal impacts.

Table 13. Results of dry density range analysis.

Index		Factors								
		A	B	C	D	E	F	G	H	Empty Column
Dry Density (kg/m^3)	K_{11}	4774.53	4798.98	4927.13	4968.90	4766.83	4831.29	4796.23	4746.49	4790.03
	K_{12}	4778.42	4766.03	4836.45	4931.66	4754.90	4774.60	4735.01	4789.31	4789.73
	K_{13}	4777.99	4769.53	4728.79	4635.85	4781.93	4749.58	4749.11	4773.36	4795.16
	K_{14}	4772.68	4769.08	4611.25	4567.21	4799.96	4748.15	4823.27	4794.46	4789.77
	k_{11}	596.82	599.87	615.89	621.11	595.85	603.91	599.53	593.31	598.75
	k_{12}	597.30	595.75	604.56	616.46	594.36	596.83	591.88	598.66	598.72
	k_{13}	597.25	596.19	591.10	579.48	597.74	593.70	593.64	596.67	599.40
	k_{14}	596.59	596.14	576.41	570.90	600.00	593.52	602.91	599.31	598.72
R		0.72	4.12	39.49	50.21	5.63	10.39	11.03	6.00	0.68
Optimal Level		2	1	1	1	4	1	4	4	

Note: K_{ij} represents the sum of test results corresponding to level *j* in any factor column under the performance index *i*. k_{ij} denotes the average value of test results for level number *j* in any factor column.

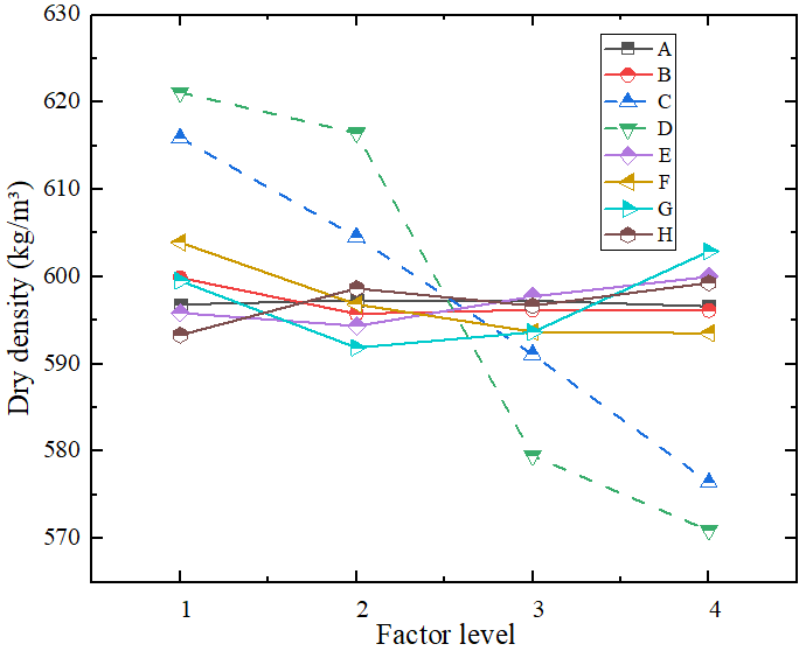


Figure 9. Dry density of AAFC varies with the levels of various factors.

(2) Range Analysis of Thermal Conductivity

As shown in Table 14, the thermal conductivity decreases with the increasing foam and aerogel content. The curve slope for aerogel content is the steepest, indicating the greatest influence magnitude, significantly exceeding the other factors (Figure 10). The increase in foam content from the low to high level merely reduces the thermal conductivity by 5.55%, whereas the incorporation of aerogel results in a more substantial reduction of 19.77%. This demonstrates that aerogel, as a super-insulating material, can remarkably reduce the thermal conductivity of FC. Foam content is the next most influential factor, and is well documented [39–41]. Other factors exert minimal effects.

Table 14. Results of thermal conductivity range analysis.

Index		Factors								
		A	**B**	**C**	**D**	**E**	**F**	**G**	**H**	**Empty Column**
Thermal Conductivity (W/(m·K))	K_{21}	0.8484	0.8486	0.8510	0.8645	0.8564	0.9671	0.8610	0.8478	0.8035
	K_{22}	0.8388	0.8169	0.8421	0.8422	0.8426	0.8113	0.8310	0.8358	0.7887
	K_{23}	0.8430	0.8447	0.8484	0.8319	0.8236	0.8010	0.8371	0.8233	0.8049
	K_{24}	0.8254	0.8454	0.8141	0.8170	0.8330	0.7761	0.8265	0.8486	0.7885
	k_{21}	0.1060	0.1061	0.1064	0.1081	0.1071	0.1209	0.1076	0.1060	0.1004
	k_{22}	0.1049	0.1021	0.1053	0.1053	0.1053	0.1014	0.1039	0.1045	0.0986
	k_{23}	0.1054	0.1056	0.1060	0.1040	0.1029	0.1001	0.1046	0.1029	0.1006
	k_{24}	0.1032	0.1057	0.1018	0.1021	0.1041	0.0970	0.1033	0.1061	0.0986
R		0.0029	0.0040	0.0046	0.0059	0.0041	0.0239	0.0043	0.0032	0.0021
Optimal Level		4	2	4	4	3	4	4	3	

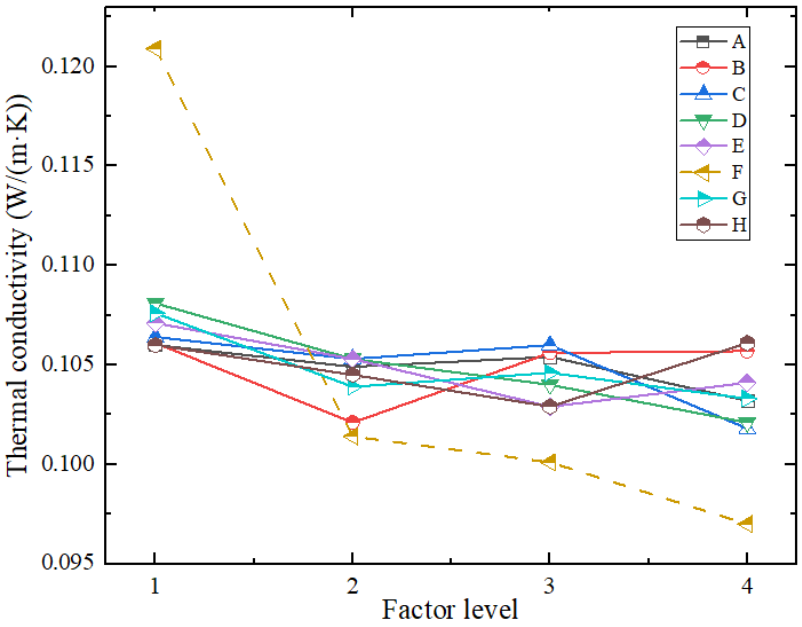


Figure 10. Thermal conductivity of AAFC varies with the levels of various factors.

(3) Mass Water Absorption Rate

Analysis of the range values (R) (Table 15) and curves in Figure 11 shows that the waterproofing agent dosage is the most significant factor affecting the mass water absorption rate, which decreases significantly with increasing dosage. Compared with previous studies, the waterproofing performance has been effectively improved [10]. Foam content is the next most influential factor, although the range value (R) of the former is approximately 2.7 times that of the latter. A higher foam content introduces more air bubbles into the solid matrix, which increases the porosity and degrades the mechanical properties. An increase in foam content raises the porosity, which in turn leads to an increase in water absorption and also reduces both mechanical and frost resistance. When the dosage is increased from Level 1 to Level 4, the mass water absorption increases by 14.24%. In contrast, the addition of a waterproofing agent reduces it by 29.22%. Factors such as activator modulus, water–binder ratio, and calcium hydroxide content show negligible effects.

Table 15. Results of mass water absorption rate range analysis.

Index		Factors								
		A	**B**	**C**	**D**	**E**	**F**	**G**	**H**	**Empty Column**
Mass Water Absorption Rate(%)	K_{31}	107.210	107.416	106.121	98.576	102.751	107.851	106.806	127.835	108.301
	K_{32}	109.207	101.146	96.030	105.642	109.775	106.910	103.246	109.090	103.271
	K_{33}	102.181	103.661	109.311	102.950	106.476	103.552	107.170	92.385	106.46
	K_{34}	101.185	107.560	108.321	112.615	100.781	101.470	102.561	90.473	101.751
	k_{31}	13.401	13.427	13.265	12.322	12.844	13.481	13.351	15.979	13.538
	k_{32}	13.651	12.643	12.004	13.205	13.722	13.364	12.906	13.636	12.909
	k_{33}	12.773	12.958	13.664	12.869	13.310	12.944	13.396	11.548	13.308
	k_{34}	12.648	13.445	13.540	14.077	12.598	12.684	12.820	11.309	12.719
R		1.003	0.802	1.660	1.755	1.124	0.798	0.576	4.670	0.819
Optimal Level		4	2	2	1	4	4	4	4	

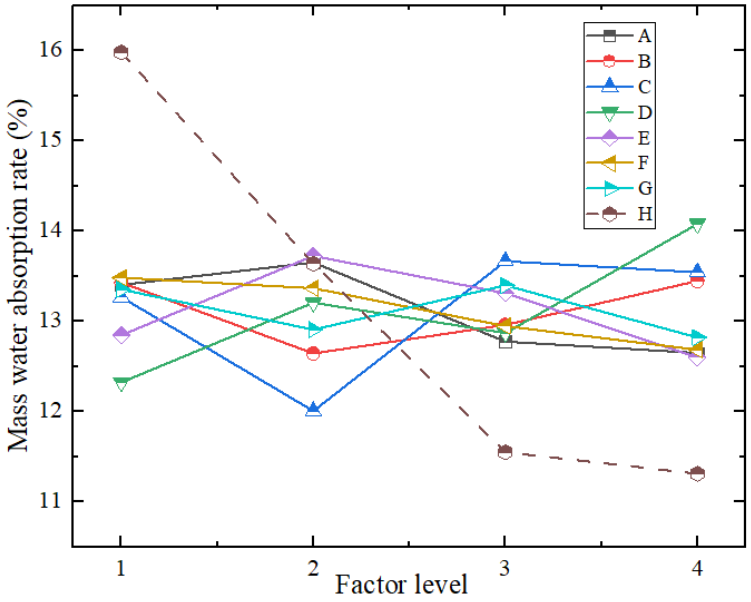


Figure 11. Water absorption of AAFC varies with the levels of various factors.

(4) Mechanical Properties

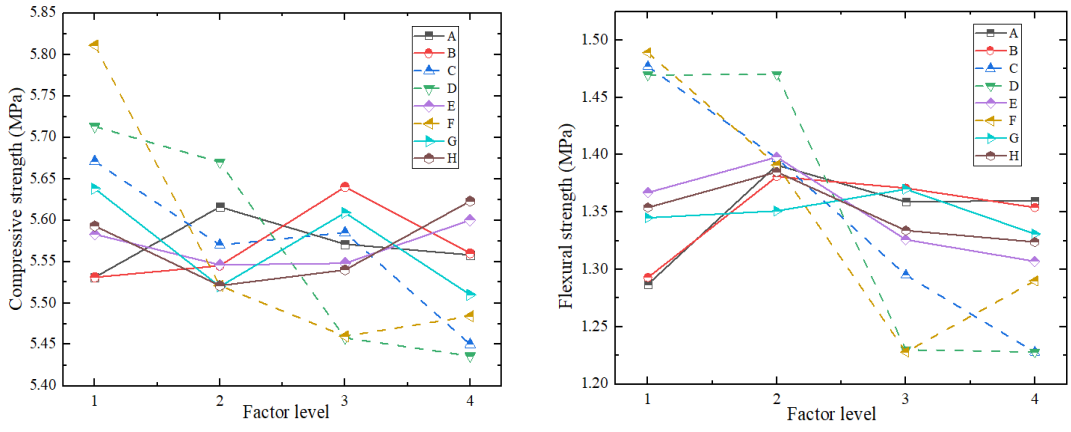
Analysis of the range values (R) for compressive and flexural strengths (Tables 16 and 17) reveals that aerogel content, foam content, and water–binder ratio are the three most influential factors. The foam stabilizer dosage has the least significant effect on the compressive strength, while calcium hydroxide content has a relatively minor influence on the flexural strength. As shown in the curves in Figure 12, both the compressive and flexural strengths decrease significantly with increasing foam content, aerogel content, and water–binder ratio. A comparative analysis reveals that from Level 1 to Level 4, the compressive strength is reduced by only 5.61% with the addition of aerogel, while the thermal conductivity is decreased by 19.77%. In contrast, increasing the foam content leads to a reduction in compressive strength of 4.84%, and the thermal conductivity is lowered by only 5.55%. Moreover, the water absorption is increased by 14.24% with higher foam content.

Table 16. Results of compressive strength range analysis.

Index		Factors								
		A	**B**	**C**	**D**	**E**	**F**	**G**	**H**	**Empty Column**
Compressive Strength (MPa)	K_{41}	44.25	44.25	45.37	45.7	44.66	46.49	45.1	44.74	45.15
	K_{42}	44.93	44.36	44.56	45.36	44.37	44.17	44.16	44.17	45.44
	K_{43}	44.57	45.12	44.68	43.66	44.38	43.68	44.87	44.32	45.51
	K_{44}	44.46	44.48	43.6	43.49	44.8	43.87	44.08	44.98	45.12
	k_{41}	5.531	5.531	5.671	5.713	5.583	5.811	5.638	5.593	5.644
	k_{42}	5.616	5.545	5.570	5.670	5.546	5.521	5.520	5.521	5.680
	k_{43}	5.571	5.640	5.585	5.458	5.548	5.460	5.609	5.540	5.689
	k_{44}	5.558	5.560	5.450	5.436	5.600	5.484	5.510	5.623	5.640
R		0.085	0.109	0.221	0.276	0.054	0.351	0.128	0.101	0.049
Optimal Level		2	3	1	1	4	1	1	4	

Table 17. Results of flexural strength range analysis.

Index		Factors								
		A	**B**	**C**	**D**	**E**	**F**	**G**	**H**	**Empty Column**
Flexural Strength (MPa)	K_{51}	10.30	10.34	11.82	11.76	10.94	11.91	10.76	10.83	11.21
	K_{52}	11.13	11.04	11.18	11.76	11.18	11.13	10.81	11.08	11.31
	K_{53}	10.88	10.97	10.36	9.84	10.61	9.82	10.96	10.67	11.33
	K_{54}	10.88	10.83	9.83	9.82	10.46	10.32	10.65	10.60	10.99
	k_{51}	1.287	1.293	1.477	1.469	1.367	1.489	1.345	1.354	1.401
	k_{52}	1.391	1.381	1.397	1.4701	1.398	1.391	1.351	1.385	1.414
	k_{53}	1.359	1.371	1.295	1.230	1.326	1.228	1.370	1.334	1.416
	k_{54}	1.360	1.354	1.228	1.228	1.307	1.290	1.331	1.324	1.373
R		0.104	0.088	0.249	0.243	0.090	0.261	0.039	0.061	0.043
Optimal Level		2	2	1	2	2	1	3	2	



(**a**) Compressive strength (**b**) Flexural strength

Figure 12. Mechanical properties of AAFC vary with the levels of various factors.

The hydration products (C(N)-A-S-H) are critical for the strength development of AAFC [42,43]. Appropriate addition of calcium hydroxide can increase the proportion of C-A-S-H in the hydration products [44], thereby improving the mechanical properties. The peak intensity associated with the C,N-A-S-H gel is enhanced with increasing calcium hydroxide dosage, as shown by FTIR analysis. The effect of foam stabilizer dosage on

the mechanical properties follows a pattern of first decreased and then increased. As a surfactant, an appropriate amount of stabilizer improves the stability of bubble membranes, prolongs their rupture half-life, and controls the bubble uniformity, size, and quantity in the slurry to enhance the mechanical properties [45].

It is found that the foam content is the primary factor governing drying shrinkage through range analysis (Table 18). The water–binder ratio exhibits a secondary influence, and the contributions of remaining factors are marginal. The shrinkage is induced by the solid matrix, whereas the solid volume fraction is reduced with increased porosity. As shown in Figure 13, the drying shrinkage decreases nearly linearly with the increasing foam content, which is attributable to the increased porosity, which reduces the solid phase fraction and thus the autogenous shrinkage of the AA matrix. In contrast, drying shrinkage increases with the water–binder ratio; higher ratios improve workability but also increase macroporosity and connectivity, accelerating moisture loss and capillary evaporation. When the foam content is increased from the lowest to the highest level, the drying shrinkage is reduced by 31.88%. In contrast, an increase in the water–binder ratio causes it to rise by 16.12%. The resulting capillary pressure difference further intensifies the shrinkage stress.

Table 18. Results of drying shrinkage range analysis.

Index		Factors								
		A	**B**	**C**	**D**	**E**	**F**	**G**	**H**	**Empty Column**
Drying Shrinkage (mm/m)	K_{61}	6.144	6.087	5.609	7.352	6.221	6.056	6.082	6.131	6.11
	K_{62}	6.175	6.103	6.131	6.545	6.137	6.159	6.077	6.139	6.103
	K_{63}	6.05	6.284	6.256	5.602	6.017	6.089	6.135	6.081	6.105
	K_{64}	6.137	6.032	6.51	5.007	6.131	6.202	6.212	6.155	6.049
	k_{61}	0.768	0.761	0.701	0.919	0.778	0.757	0.7603	0.766	0.764
	k_{62}	0.772	0.763	0.766	0.818	0.767	0.770	0.7596	0.767	0.763
	k_{63}	0.756	0.786	0.782	0.700	0.752	0.761	0.767	0.760	0.763
	k_{64}	0.767	0.754	0.814	0.626	0.766	0.775	0.777	0.769	0.756
R		0.016	0.031	0.113	0.293	0.026	0.018	0.017	0.009	0.008
Optimal Level		3	4	1	4	3	1	2	3	

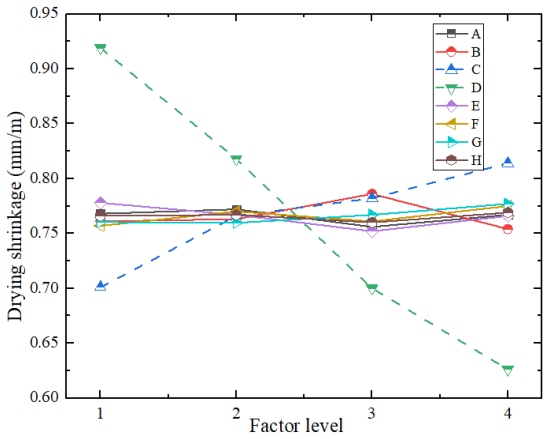


Figure 13. Drying shrinkage of AAFC varies with the level of various factors.

(5) Frost Resistance

The range calculation and analysis results of the strength loss rate and mass loss rate are listed in Tables 19 and 20:

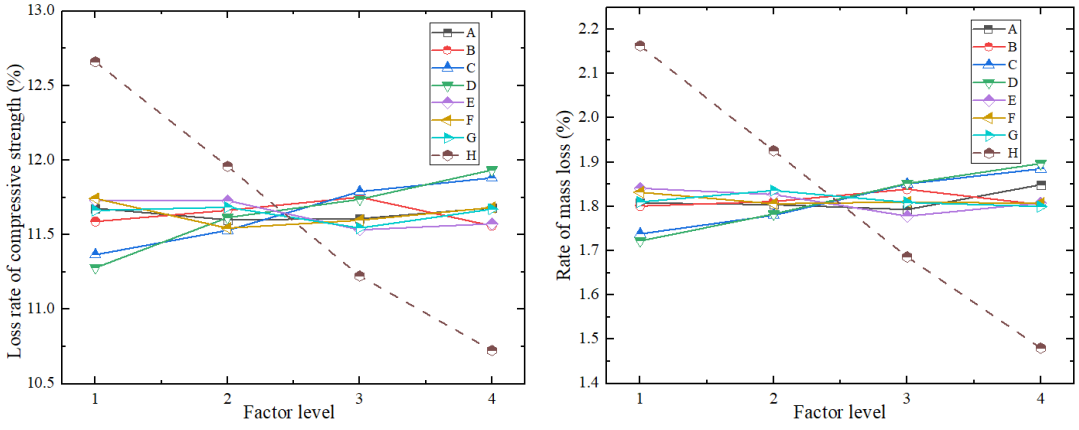
Table 19. Results of strength loss rate range analysis.

Index		Factors								
		A	**B**	**C**	**D**	**E**	**F**	**G**	**H**	**Empty Column**
Strength Loss Rate (%)	K_{71}	93.414	92.712	90.927	90.227	93.846	93.941	93.301	101.276	93.958
	K_{72}	92.801	93.310	92.228	92.917	93.830	92.350	93.475	95.669	93.409
	K_{73}	92.863	94.015	94.313	93.899	92.261	92.774	92.363	89.780	93.333
	K_{74}	93.440	92.481	95.050	95.475	92.581	93.453	93.379	85.793	93.818
	k_{71}	11.677	11.589	11.366	11.278	11.731	11.743	11.663	12.660	11.745
	k_{72}	11.600	11.664	11.529	11.615	11.729	11.544	11.684	11.959	11.676
	k_{73}	11.608	11.752	11.789	11.737	11.533	11.597	11.545	11.223	11.667
	k_{74}	11.680	11.560	11.881	11.934	11.573	11.682	11.672	10.724	11.727
R		0.080	0.192	0.515	0.656	0.198	0.199	0.139	1.935	0.078
Optimal Level		2	4	1	1	3	2	3	4	

Table 20. Results of mass loss rate range analysis.

Index		Factors								
		A	**B**	**C**	**D**	**E**	**F**	**G**	**H**	**Empty Column**
Mass Loss Rate (%)	K_{81}	14.466	14.407	13.902	13.777	14.724	14.653	14.478	17.301	14.523
	K_{82}	14.43	14.484	14.24	14.26	14.617	14.447	14.691	15.411	14.556
	K_{83}	14.347	14.71	14.81	14.817	14.225	14.478	14.468	13.485	14.308
	K_{84}	14.79	14.432	15.081	15.179	14.467	14.455	14.396	11.836	14.377
	k_{81}	1.808	1.801	1.738	1.722	1.841	1.832	1.810	2.163	1.815
	k_{82}	1.804	1.811	1.780	1.783	1.827	1.806	1.836	1.926	1.820
	k_{83}	1.793	1.839	1.851	1.852	1.778	1.810	1.809	1.686	1.789
	k_{84}	1.849	1.804	1.885	1.897	1.808	1.807	1.800	1.480	1.797
R		0.055	0.038	0.147	0.175	0.062	0.026	0.037	0.683	0.031
Optimal Level		3	1	1	1	3	2	4	4	

By comparing the range values (R), it can be seen that the three most influential factors on the freezing resistance of the AAFC are, in the following order: waterproofing agent dosage, foam content, and water–binder ratio. The other factors have relatively minor effects (Figure 14).



(**a**) Strength loss rate (**b**) Mass loss rate

Figure 14. Frost resistance of AAFC varies with the levels of various factors.

The frost resistance shows a strong correlation with mass water absorption. The dosage of the waterproofing agent demonstrates the most significant effect on frost resistance, with both the strength and mass loss rates decreasing approximately linearly as its content increases. The frost resistance is highly correlated with mass water absorption. It is improved by 31.57% with an increased dosage of the waterproofing agent. Reduced water absorption causes this improvement. It mitigates the 9% volumetric expansion of water upon freezing. Thereby, frost-heave pressure inside the pores is lowered. However, increased foam content reduces frost resistance. It makes the material more porous, coarsens pores, and thins walls. This elevates water absorption and aggravates frost damage. Similarly, a raised water–binder ratio weakens frost resistance. It enhances slurry fluidity and alters pore traits. Thus, internal stress differences arise between saturated and unsaturated zones during freeze–thaw.

4.3.2. Analysis of Variance (ANOVA) of Test Results

Range analysis of orthogonal test results can effectively determine the primary and secondary orders of influencing factors, but it cannot distinguish data fluctuations caused by changes in test conditions and errors, nor evaluate the significance level of the influencing factors. Therefore, ANOVA was conducted. The significance of the influence of each factor can be determined by constructing an F-statistic for the F-test. The F-test can be divided into four cases: F > F0.01,indicating that the factor has an extremely significant effect, denoted by "**"; F0.01 $\geq$ F > F0.05, indicating that the factor has a significant effect, denoted by "*"; F0.05 $\geq$ F > F0.1, indicating that the factor has a certain degree of effect, denoted by "(*)"; F0.1 > F, indicating that the factor has a minimal effect, with no marking used.

The range and variance analysis results in Table 21 show good consistency. A comprehensive analysis of both methods leads to the following conclusions:

Table 21. Results of the variance analysis of the orthogonal test.

Index	Source of Variance	Sum of Squared Deviations		Degree of Freedom	Mean Square Ms	F Value	Significance
Dry Density (kg/m^3)	A	SS_A	2.870	3	0.957	0.044	
	B	SS_B	89.649	3	29.883	1.365	
	C	SS_C	6983.224	3	2327.741	106.320	**
	D	SS_D	15,584.462	3	5194.821	237.275	**
	E	SS_E	142.314	3	47.438	2.167	
	F	SS_F	566.568	3	188.856	8.626	(*)
	G	SS_G	630.865	3	210.288	9.605	*
	H	SS_H	174.463	3	58.154	2.656	
	Error E	SS_E	65.681	3	21.894		
	Sum	SS_T	24,240.096	31			
Thermal Conductivity (W/(m·K))	A	SS_A	3.59384×10^{-5}	3	1.198×10^{-5}	2.7289	
	B	SS_B	8.13828×10^{-5}	3	2.713×10^{-5}	6.1796	(*)
	C	SS_C	0.000107308	3	3.577×10^{-5}	8.1481	(*)
	D	SS_D	0.000149903	3	4.997×10^{-5}	11.3825	*
	E	SS_E	7.37212×10^{-5}	3	2.457×10^{-5}	5.5978	(*)
	F	SS_F	0.002821489	3	0.0009405	214.2426	**
	G	SS_G	8.81847×10^{-5}	3	2.939×10^{-5}	6.6961	(*)
	H	SS_H	5.35474×10^{-5}	3	1.785×10^{-5}	4.0660	
	Error E	SS_E	1.32×10^{-5}	3	4.39×10^{-6}		
	Sum	SS_T	0.003425	31			

Table 21. *Cont.*

Index	Source of Variance	Sum of Squared Deviations		Degree of Freedom	Mean Square Ms	F Value	Significance
Mass Water Absorption Rate(%)	A	SS_A	18.2856	3	6.0952	8.5416	(*)
	B	SS_B	16.3877	3	5.4626	7.6550	(*)
	C	SS_C	45.2873	3	15.0958	21.1547	*
	D	SS_D	57.3406	3	19.1135	26.7850	*
	E	SS_E	31.0806	3	10.3602	14.5184	*
	F	SS_F	12.6851	3	4.2284	5.9255	(*)
	G	SS_G	9.5971	3	3.1990	4.4830	
	H	SS_H	80.2010	3	26.7337	37.4636	**
	Error E	SS_E	2.141	3	0.714		
	Sum	SS_T	273.0056	31			
Compressive Strength (MPa)	A	SS_A	0.0335	3	0.0112	9.8946	*
	B	SS_B	0.0436	3	0.0145	12.8866	*
	C	SS_C	0.2581	3	0.0860	76.2713	**
	D	SS_D	0.3975	3	0.1325	117.4714	**
	E	SS_E	0.0165	3	0.0055	4.8859	
	F	SS_F	0.4868	3	0.1623	143.8448	**
	G	SS_G	0.0281	3	0.0094	8.3063	(*)
	H	SS_H	0.0304	3	0.0101	8.9712	(*)
	Error E	SS_E	0.0034	3	0.0011		
	Sum	SS_T	1.2979	31			
Flexural Strength (MPa)	A	SS_A	0.2966	3	0.0989	29.0104	*
	B	SS_B	0.1443	3	0.0481	14.1092	*
	C	SS_C	0.3822	3	0.1274	37.3773	**
	D	SS_D	0.3745	3	0.1248	36.6244	**
	E	SS_E	0.2225	3	0.0742	21.7644	*
	F	SS_F	0.4065	3	0.1355	39.7534	**
	G	SS_G	0.0900	3	0.0300	8.7988	(*)
	H	SS_H	0.0943	3	0.0314	9.2191	(*)
	Error E	SS_E	0.0102	3	3.41×10^{-3}		
	Sum	SS_T	2.0210	31			
Drying Shrinkage (mm/m)	A	SS_A	0.0349	3	0.0116	2.0999	
	B	SS_B	0.1196	3	0.0399	7.2035	(*)
	C	SS_C	0.1311	3	0.0437	7.8952	(*)
	D	SS_D	0.4267	3	0.1422	25.6941	*
	E	SS_E	0.0486	3	0.0162	2.9261	
	F	SS_F	0.0413	3	0.0138	2.4885	
	G	SS_G	0.0382	3	0.0127	2.3019	
	H	SS_H	0.0295	3	0.0098	1.7760	
	Error E	SS_E	0.0166	3	0.0055		
	Sum	SS_T	0.8866	31			
Strength Loss Rate (%)	A	SS_A	7.2638	3	2.4213	5.0263	
	B	SS_B	11.8639	3	3.9546	8.2094	(*)
	C	SS_C	20.5288	3	6.8429	14.2052	*
	D	SS_D	21.6072	3	7.2024	14.9514	*
	E	SS_E	14.2014	3	4.7338	9.8269	*
	F	SS_F	12.1380	3	4.0460	8.3990	(*)
	G	SS_G	9.3936	3	3.1312	6.5000	(*)
	H	SS_H	45.0139	3	15.0046	31.1481	**
	Error E	SS_E	1.4452	3	0.4817		
	Sum	SS_T	143.4557	31			
Mass Loss Rate (%)	A	SS_A	0.2816	3	0.0939	8.4316	(*)
	B	SS_B	0.2977	3	0.0992	8.9154	(*)
	C	SS_C	0.9241	3	0.3080	27.6718	*
	D	SS_D	1.0934	3	0.3645	32.7423	**
	E	SS_E	0.3931	3	0.1310	11.7724	*
	F	SS_F	0.1694	3	0.0565	5.0716	
	G	SS_G	0.2258	3	0.0753	6.7621	(*)
	H	SS_H	1.9874	3	0.6625	59.5113	**
	Error E	SS_E	0.3339	3	0.1113		
	Sum	SS_T	5.7064	31			

(1) The foam content significantly affects all properties, reducing the thermal conductivity slightly, but increasing water absorption and shrinkage while compromising

mechanical and frost resistance. The increase in foam content, however, leads to a greater degradation of other key properties. Thus, controlling its dosage is essential.

(2) The aerogel content exhibits an extremely significant effect on thermal performance. Combining the increased aerogel content with moderately reduced foam content simultaneously enhances the thermal and mechanical properties.

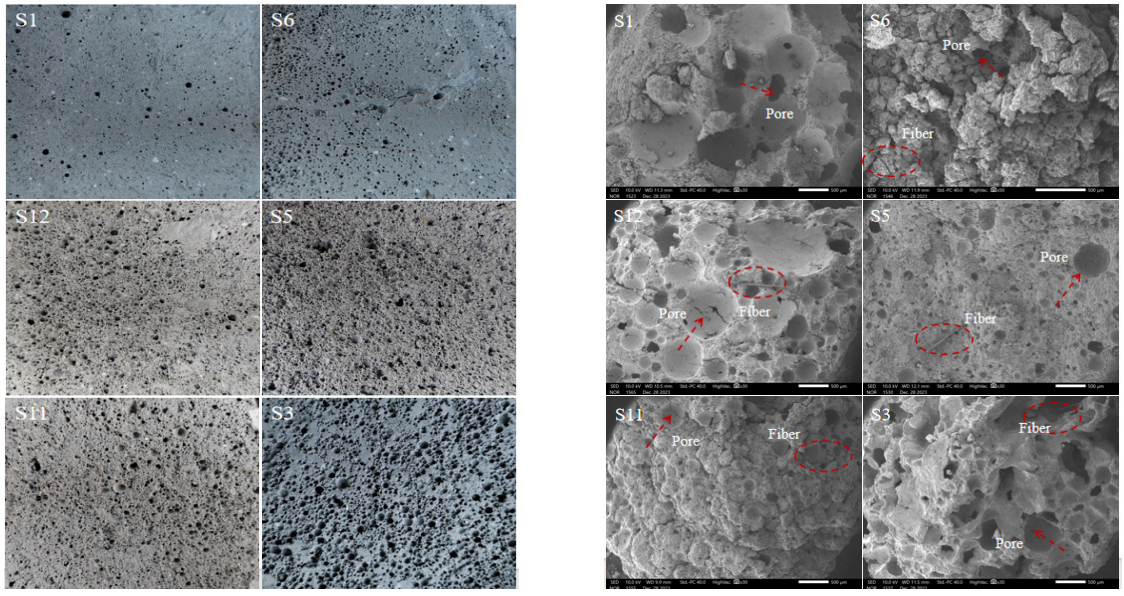
(3) The water–binder ratio significantly influences the mechanical properties and density, with significant effects on water absorption and frost resistance. Its complex effects necessitate careful optimization.

(4) Calcium hydroxide moderately improves the mechanical properties through an initial-decrease-then-increase pattern, while showing negligible effects on other parameters.

(5) The waterproofing agent significantly enhances the water resistance and frost durability, slightly improves the mechanical properties, and minimally affects the thermal and density characteristics.

4.3.3. Microscopic Analysis

Variations in mix proportions significantly affect the micro-morphology of the specimens (Figure 15). An overall increasing trend in pore size and porosity is observed across the six specimen groups. Specimen S3 exhibits the largest pore size, along with the lowest thermal conductivity and dry density. In contrast, the opposite trend is noted for Specimen S1. This trend strongly correlates with pore size and its characteristics [46,47], indicating that foam content and water-to-binder ratio considerably influence pore structure. Although Specimens S5 and S11 differ in water-to-binder ratio and foam content, their low thermal conductivity is attributed to high aerogel content, confirming aerogel as a key influencing factor. SEM images reveal that Specimen S3 is characterized by high porosity and thin pore walls. With a higher dosage of foam stabilizer, Specimen S11 exhibits fewer interconnected pores and more uniform pore sizes [48]. The random dispersion of basalt fibers contributes to enhanced mechanical properties. No independent fly ash particles were observed.



(**a**) (**b**)

Figure 15. Morphologies of samples with different mix ratios. (**a**) Changes in the appearance of samples with different formulations. (**b**) Changes in the microstructure of samples with different formulations (SEM).

FTIR analysis (Figure 16) indicates that the absorption peak in the wavenumber range of 1000–1040 cm^{-1} corresponds to the asymmetric stretching vibration of Si-O-X (Na/Al). This peak is identified as the most prominent characteristic absorption peak of the AAFC [49]. Variations in the intensity of this absorption peak are observed among the six specimen groups. A stronger and sharper peak suggests a higher content of hydrated sodium (calcium) aluminosilicate (C,N-A-S-H) in the reaction products. This is beneficial for enhancing the mechanical properties of FC [50,51]. Furthermore, compared with the infrared spectrum of raw FA, the characteristic Si-O-X (Na/Al) peak in the products is shifted to a lower wavenumber. This shift reflects a gradual increase in C,N-A-S-H gel products [25,29]. The extent of this peak shift varies due to differences in alkali concentration among the systems with different mix proportions. The peak at 1430 cm^{-1} is assigned to the asymmetric stretching vibration of carbonate. The strongest peak for S11 was detected at this position. As S11 had the highest alkali equivalent among all mix proportions, its system exhibited strong alkalinity, indicating maximum carbonate formation. Additionally, two characteristic peaks are present at 3433 cm^{-1} and 1630 cm^{-1}. They correspond to the bending vibration of H-O-H bonds. The peak at 1630 cm^{-1} is characterized as the signature of bound water in cementitious materials [52].

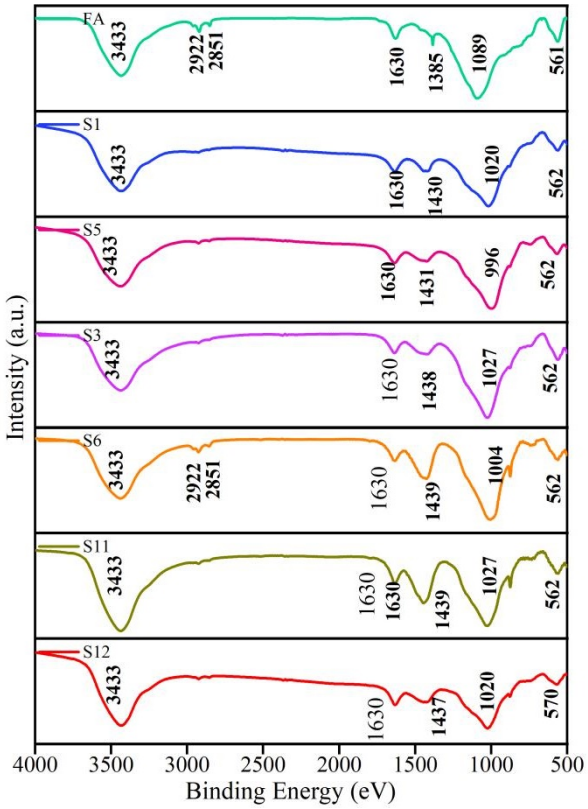


Figure 16. FTIR diagram of samples with different mix ratios.

The chemical analysis results are corroborated by the micro-morphology observed via SEM. For instance, the stronger carbonate peak (1430 cm^{-1}) and the pronounced shift in the main Si–O–X peak in S11 indicate high alkalinity and a well-developed gelation degree in its system. This finding is consistent with its SEM images, which show a structure with fewer interconnected pores and more uniform pore sizes [49]. It can be inferred that sufficient alkali activation promotes the formation of a denser and more homogeneous microstructure. In contrast, specimens with high porosity and thin pore walls, such as S3, likely correspond to different gel product characteristics and moisture states in their FTIR spectra. These factors collectively determine their macroscopic thermal and mechanical

properties. Furthermore, the dispersion of basalt fibers and the absence of unreacted FA particles are confirmed by the microscopic morphology.

4.4. Determination of Optimal Mix Proportion for AAFC

4.4.1. Mix Proportion Optimization Method

Both range and variance analyses are single-factor analysis methods that cannot determine the optimal mix proportion under multi-factor conditions in orthogonal experiments. The matrix analysis method can objectively conduct a comprehensive analysis of multi-factor and multi-index systems and calculate the weights of each factor level. Therefore, matrix analysis was used to determine the optimal mix proportion for the AAFC.

Based on the orthogonal experimental scheme and the performance index system of the AAFC, a three-layer hierarchical structure model was constructed, including the index, factor, and level layers. The model consists of eight factors with four levels each, and eight performance indicators were investigated. The constructed structural model is presented in the following Table 22:

Table 22. Orthogonal test of the AAFC data structure model.

Index Layer	**Performance Indicators**													
Factor Layer	**Factor A**				**Factor B**				···	**Factor H**				
Level Layer	A_1	A_2	A_3···	A_4	B_1	B_2	B_3···	B_4	···	H_1	H_2	H_3···	H_4	

Index Layer Matrix: The average value of the test index for factor X_i at the j level is defined as m_{ij}. For indicators in which larger values indicate better performance, $M_{ij} = m_{ij}$; for indicators in which smaller values are preferable, $M_{ij} = 1/m_{ij}$. The established index matrix is expressed by Equation (8):

$$M = \begin{bmatrix} M_{11} & 0 & 0 & \cdots & 0 \\ M_{12} & 0 & 0 & \cdots & 0 \\ \cdots & \cdots & \cdots & \cdots & \cdots \\ M_{1m} & 0 & 0 & \cdots & 0 \\ 0 & M_{21} & 0 & \cdots & 0 \\ 0 & M_{22} & 0 & \cdots & 0 \\ \cdots & \cdots & \cdots & \cdots & \cdots \\ 0 & M_{2m} & 0 & \cdots & 0 \\ 0 & 0 & 0 & \cdots & 0 \\ 0 & 0 & 0 & \cdots & M_{l1} \\ 0 & 0 & 0 & \cdots & M_{l1} \\ \cdots & \cdots & \cdots & \cdots & \cdots \\ 0 & 0 & 0 & \cdots & M_{lm} \end{bmatrix} \quad (8)$$

Factor Layer Matrix: Let $T_i = \frac{1}{\sum_{j=1}^{m} M_{ij}}$, the factor matrix is established as shown in Equation (9):

$$T = \begin{bmatrix} T_1 & 0 & \cdots & 0 \\ 0 & T_2 & \cdots & 0 \\ \cdots & \cdots & \cdots & \cdots \\ 0 & 0 & \cdots & T_l \end{bmatrix} \quad (9)$$

Level Layer Matrix: Calculate the range S_i of factor A_i, let $S_i = \frac{s_i}{\sum_{i=1}^{l} s_i}$; the factor matrix is established as shown in Equation (10):

$$S = \begin{bmatrix} S_1 \\ S_2 \\ \cdots \\ S_l \end{bmatrix} \tag{10}$$

Weight Matrix: For the weight matrix of the factors influencing the test indices $\omega_i = M_i T_i S_i$, ω_i^T can be expressed as follows:

$$\omega_i^T = [\omega_1, \omega_2, \mathrm{L}, \omega_\mathrm{m}] \tag{11}$$

The total weight matrix was obtained by averaging the sum of the weight matrices for each factor ω_i, as shown in Equation (12):

$$\omega^\mathrm{T} = \left(\omega_1^\mathrm{T} + \omega_2^\mathrm{T} + \mathrm{L} + \omega_x^\mathrm{T}\right)/l \tag{12}$$

4.4.2. Analysis and Determination of Optimal Mix Proportion

The weight matrix for eight performance indicators, including dry density, was calculated based on the established three-layer hierarchical structure model. For five indicators (thermal conductivity, mass water absorption rate, drying shrinkage, strength loss rate, and mass loss rate), smaller values are preferable; therefore, $M_{ij} = 1/m_{ij}$ is adopted. For dry density, compressive strength, and flexural strength (where larger values are preferable), $M_{ij} = 1/m_{ij}$ is used. The calculation results based on this method are listed in the following Table 23:

Table 23. Results of matrix analysis.

Factors	ρ	λ	Wr	f	R_f	ε	F_c	M_m	Total Weight
A_1	0.001406	0.001355	0.019789	0.015929	0.021806	0.007451	0.005086	0.011342	0.010521
A_2	0.001405	0.001371	0.019427	0.016174	0.023565	0.007413	0.005119	0.011370	0.010731
A_3	0.001405	0.001364	0.020763	0.016044	0.023033	0.007567	0.005116	0.011436	0.010841
A_4	0.001407	0.001393	0.020967	0.016004	0.023050	0.007459	0.005084	0.011093	0.010807
B_1	0.008032	0.001869	0.015798	0.020380	0.018552	0.015159	0.012301	0.007790	0.012485
B_2	0.008087	0.001941	0.016777	0.020430	0.019814	0.015119	0.012222	0.007748	0.012767
B_3	0.008081	0.001878	0.016370	0.020780	0.019673	0.014684	0.012131	0.007629	0.012653
B_4	0.008082	0.001876	0.015777	0.020485	0.019428	0.015297	0.012332	0.007776	0.012632
C_1	0.074948	0.002170	0.033044	0.042511	0.059972	0.058656	0.033702	0.031382	0.042048
C_2	0.076354	0.002193	0.036516	0.041752	0.056736	0.053662	0.033227	0.030637	0.041385
C_3	0.078092	0.002177	0.032080	0.041865	0.052582	0.052590	0.032492	0.029458	0.040167
C_4	0.080083	0.002269	0.032373	0.040853	0.049872	0.050538	0.032240	0.028928	0.039645
D_1	0.094436	0.002759	0.037616	0.053465	0.058186	0.114342	0.043226	0.037643	0.055209
D_2	0.095149	0.002832	0.035100	0.053067	0.058202	0.128440	0.041975	0.036368	0.056392
D_3	0.101221	0.002867	0.036018	0.051078	0.048713	0.150061	0.041536	0.035001	0.058312
D_4	0.102742	0.002919	0.032927	0.050880	0.048599	0.167893	0.040850	0.034166	0.060122

Table 23. *Cont.*

Factors	ρ	λ	Wr	f	R_f	ε	F_c	M_m	Total Weight
E_1	0.011058	0.001923	0.023148	0.010166	0.020177	0.012008	0.012556	0.012551	0.012948
E_2	0.011085	0.001954	0.021667	0.010100	0.020630	0.012173	0.012558	0.012643	0.012851
E_3	0.011023	0.001999	0.022339	0.010102	0.019567	0.012415	0.012772	0.012991	0.012901
E_4	0.010981	0.001977	0.023601	0.010198	0.019295	0.012184	0.012728	0.012774	0.012967
F_1	0.001905	0.011869	0.016304	0.064976	0.052377	0.008781	0.012750	0.005270	0.021779
F_2	0.001895	0.011718	0.015792	0.065705	0.059349	0.008681	0.012808	0.005282	0.022654
F_3	0.001873	0.009831	0.015654	0.069156	0.063528	0.008829	0.012591	0.005207	0.023334
F_4	0.001906	0.012250	0.016638	0.065258	0.055032	0.008621	0.012657	0.005279	0.022205
G_1	0.001637	0.002063	0.011381	0.024228	0.008808	0.008058	0.008951	0.007552	0.009085
G_2	0.001642	0.002078	0.011814	0.023845	0.008684	0.008135	0.008845	0.007438	0.009060
G_3	0.001621	0.002006	0.011420	0.024352	0.008646	0.008129	0.008861	0.007547	0.009073
G_4	0.001612	0.002090	0.011893	0.023801	0.008555	0.007959	0.008854	0.007590	0.009044
H_1	0.001672	0.001500	0.075879	0.019184	0.013437	0.004420	0.113216	0.114664	0.042996
H_2	0.001657	0.001521	0.088917	0.018940	0.013747	0.004415	0.119851	0.128726	0.047222
H_3	0.001662	0.001545	0.104995	0.019004	0.013241	0.004457	0.127713	0.147112	0.052466
H_4	0.001655	0.001498	0.107214	0.019287	0.013144	0.004403	0.133648	0.167607	0.056057

Based on the above results, the optimal mix proportion of AAFC was determined to be $A_3B_2C_1D_4E_4F_3G_1H_4$, with the following factor levels: alkali equivalent of 0.1, activator modulus of 1.1, water-to-binder ratio of 0.4, foam dosage of 4.5 (multiple of theoretical value), foam stabilizer dosage of 3.5% (by mass of foaming agent), aerogel dosage of 6 kg/m^3, calcium hydroxide dosage of 5% (by mass of FA), and waterproofing agent dosage of 5.5% (by mass of FA). The specimens were prepared and cured again according to the above mix proportion, and the performance parameters of the optimal mix AAFC were measured as follows: dry density of 576.34 kg/m^3, thermal conductivity of 0.1107 W/(m·K), mass water absorption rate of 3.87%, compressive strength of 5.83 MPa, flexural strength of 1.41 MPa, drying shrinkage of 0.614 mm/m, strength loss rate of 10.433%, and mass loss rate of 1.764%. This indicates that all the indicators of the AAFC with the optimal mix proportion meet the target requirements.

5. Conclusions

To address the proposed research question, this study develops a high-performance AAFC insulation material. Systematic material design and process control were employed. Industrial solid waste FA served as the sole aluminosilicate source. SiO_2 aerogel was incorporated as a functional composite using alkali-activation technology. This approach successfully fabricated a novel low-carbon FC. The material demonstrates significant potential for engineering applications. All preset research objectives are successfully achieved. The main conclusions are as follows:

(1) A target performance system was established for the ultralow energy buildings in the HSCW, comprising six primary and ten secondary indicators, with particular emphasis on water resistance.

(2) A volume-based mix design method was proposed for the AAFC. Preliminary mixes only met dry density targets, with mass water absorption reaching 57.1% (11.42 times the target), indicating the need for comprehensive optimization.

(3) An 8-factor, 4-level orthogonal experiment was designed. Incorporating SiO_2 aerogel (6 kg/m^3) addresses the conventional conflict between enhancing thermal performance through increased porosity and preserving mechanical strength. This approach

effectively lowers thermal conductivity while maintaining the mechanical properties. The waterproofing agent (5.5% FA mass) achieves optimal water resistance and frost durability.

(4) The optimal mix proportion of AAFC was determined to be $A_3B_2C_1D_4E_4F_3G_1H_4$ by matrix analysis. The performance indicators are as follows: dry density 576.34 kg/m^3; thermal conductivity, 0.1107 W/(m·K); water absorption, 3.87%; compressive strength 5.83 MPa, flexural strength 1.41 MPa, drying shrinkage, 0.614 mm/m; frost resistance (10.433% strength loss and 1.764% mass loss). All parameters satisfy the target requirements.

Certainly, this study has several limitations in terms of materials, design, and processing. These limitations highlight key directions for future research. First, the fly ash (FA) used was from a single source. This does not reflect the high variability in composition and reactivity of practical FA. Future work should establish a material property database. Predictive performance models should also be developed. These steps will help formulate raw material standards and pretreatment techniques specific to AAFC. Second, the current mix design relies on single-objective optimization. This approach makes it difficult to synergistically enhance thermal and mechanical properties. There is an urgent need to introduce multi-objective optimization algorithms. Furthermore, a multi-scale "composition-structure-performance" correlation framework must be established. This knowledge can guide the development of functionally graded materials. Third, liquid alkali activators pose significant challenges. Their corrosiveness, hazardous nature, and processing complexity hinder industrial adoption. A crucial future breakthrough lies in developing solid activators or geopolymer precursor powders. The corresponding dry-mixing, stirring, and forming processes must also be systematically optimized. Additionally, the long-term durability of AAFC (e.g., freeze–thaw resistance, carbonation resistance) lacks systematic evaluation. Future studies should conduct long-term performance monitoring and investigate degradation mechanisms. Finally, a comprehensive lifecycle assessment is needed. This assessment should quantify the environmental benefits and economic feasibility of the new material system. Such analysis will provide a solid foundation for its engineering application and commercialization.

Author Contributions: Conceptualization, Y.G.; Methodology, Y.G.; Software, W.W.; Formal analysis, W.W.; Investigation, P.L.; Data curation, Y.G.; Writing—original draft, P.L.; Writing—review & editing, P.L. and W.W.; Project administration, Y.G.; Funding acquisition, P.L. All authors have read and agreed to the published version of the manuscript.

Funding: This research was supported by the Natural Science Foundation of the Jiangsu Higher Education Institutions of China (Grant No. 22KJB560014), Jiangsu Collaborative Innovation Center for Building Energy Saving and Construction Technology Youth Doctoral Foundation (Grant No. SJXTBS2107).

Data Availability Statement: The original contributions presented in the study are included in the article, further inquiries can be directed to the corresponding author.

Conflicts of Interest: The authors declare that they have no conflicts of interest.

References

1. Peráček, T.; Kaššaj, M. Legal Easements as Enablers of Sustainable Land Use and Infrastructure Development in Smart Cities. *Land* **2025**, *14*, 681. [CrossRef]
2. China Association of Building Energy Efficiency, Chongqing University. *Research Report on Carbon Emissions in China's Urban and Rural Construction Sector*, 2024th ed.; China Association of Building Energy Efficiency: Beijing, China, 2025.
3. Gencel, O.; Bayraktar, O.Y.; Kaplan, G.; Arslan, O.; Nodehi, M.; Benli, A.; Gholampour, A.; Ozbakkaloglu, T. Lightweight foam concrete containing expanded perlite and glass sand: Physico-mechanical, durability, and insulation properties. *Constr. Build. Mater.* **2022**, *320*, 126187. [CrossRef]

4. Zhang, W.; Yu, H.; Yin, B.; Akbar, A.; Dai, J.-G.; Zhang, X.; Liew, K. Effects of recycled carbon fibers on mechanical and piezoresistive properties and environmental impact in alkali-activated cementitious materials. *J. Clean. Prod.* **2024**, *450*, 141902. [CrossRef]
5. Hore, S.; Shiuly, A. Study of thermal conductivity of different types of alkali-activated concrete:a comprehensive review. *Environ. Dev. Sustain.* **2023**, *27*, 5525–5572. [CrossRef]
6. Yılmazoğlu, M.U.; Kara, H.O.; Benli, A.; Demirkıran, A.R.; Bayraktar, O.Y.; Kaplan, G. Sustainable alkali-activated foam concrete with pumice aggregate: Effects of clinoptilolite zeolite and fly ash on strength, durability, and thermal performance. *Constr. Build. Mater.* **2025**, *464*, 140160. [CrossRef]
7. Bayraktar, O.Y.; Özel, H.B.; Benli, A.; Yılmazoğlu, M.U.; Türkel, I.; Dal, B.B.; Şevik, H.; Kaplan, G. Sustainable foam concrete development: Enhancing durability and performance through pine cone powder and fly ash incorporation in alkali-activated geopolymers. *Constr. Build. Mater.* **2024**, *457*, 139422. [CrossRef]
8. Dang, J.; Tang, X.; Xiao, J.; Han, A. Influence of alkaline activator and precursor on the foam characterization and alkali-activated foamed concrete properties. *Cem. Concr. Compos.* **2024**, *145*, 105341. [CrossRef]
9. Dang, J.; Tang, X.; Xiao, J.; Duan, Z.; Han, A. Role of recycled brick powder and alkaline solution on the properties of eco-friendly alkali-activated foam concrete. *J. Clean. Prod.* **2024**, *436*, 140381. [CrossRef]
10. Benli, A. Sustainable use of waste glass sand and waste glass powder in alkali-activated slag foam concretes: Physico-mechanical, thermal insulation and durability characteristics. *Constr. Build. Mater.* **2024**, *438*, 137128. [CrossRef]
11. Xiong, Y.; Zhang, Z.; Huo, B.; Zhang, C.; Liu, C.; Zhang, Y. Uncovering the influence of red mud on foam stability and pore features in hybrid alkali-activated foamed concrete. *Constr. Build. Mater.* **2024**, *416*, 135309. [CrossRef]
12. Liu, X.; Jiang, T.; Li, C.; Wan, M.; Xuan, W.; Wang, X. Effect of Precursor Blending Ratio and Rotation Speed of Mechanically Activated Fly Ash on Properties of Geopolymer Foam Concrete. *Buildings* **2024**, *14*, 841. [CrossRef]
13. Chen, L.; Wang, Z.; Wang, Y.; Feng, J. Preparation and properties of alkali activated metakaolin-based geopolymer. *Materials* **2016**, *9*, 767. [CrossRef]
14. Wang, S.; Li, H.; Zou, S.; Zhang, G. Experimental research on a feasible rice husk/geopolymer foam building insulation material. *Energy Build.* **2020**, *226*, 110358. [CrossRef]
15. Shakouri, S.; Bayer, Z.; Erdoan, T.S. Development of silica fume-based geopolymer foams. *Constr. Build. Mater.* **2020**, *260*, 120442. [CrossRef]
16. Beskopylny, A.N.; Shcherban', E.M.; Stel'makh, S.A.; Mailyan, L.R.; Meskhi, B.; Varavka, V.; Chernil'nik, A.; Pogrebnyak, A. Improved Fly Ash Based Structural Foam Concrete with Polypropylene Fiber. *J. Compos. Sci.* **2023**, *7*, 76. [CrossRef]
17. Cui, B.; Liu, J.; Li, S.; Shen, Z. Study on preparation and properties of cement-based/geopolymer-polystyrene composite building exterior wall insulation materials. *Sci. Adv. Mater.* **2018**, *10*, 1636–1645. [CrossRef]
18. Horvat, B.; Knez, N.; Hribar, U.; König, J.; Mušič, B. Thermal insulation and flammability of composite waste polyurethane foam encapsulated in geopolymer for sustainable building envelope. *J. Clean. Prod.* **2024**, *446*, 141387. [CrossRef]
19. Huiskes, D.M.A.; Keulen, A.; Yu, Q.L.; Brouwers, H.J.H. Design and performance evaluation of ultra-lightweight geopolymer concrete. *Mater. Des.* **2016**, *89*, 516–526. [CrossRef]
20. Hao, Y.; Yang, G.; Liang, K. Development of fly ash and slag based high-strength alkali-activated foam concrete. *Cem. Concr. Compos.* **2022**, *128*, 104447. [CrossRef]
21. Masi, G.; Tugnoli, A.; Bignozzi, M.C. Lightweight alkali activated composites by direct foaming based on ceramic tile waste and fly ash. *Ceram. Int.* **2024**, *50*, 55410–55420. [CrossRef]
22. Abdullah', S.F.A.; Liew, Y.M.; Abdullah, M.M.A.B.; Heah, C.Y.; Zulkifly, K. Mechanical Properties and Thermal Conductivity of Lightweight Foamed Geopolymer Concretes. *IOP Conf. Ser. Mater. Sci. Eng.* **2019**, *551*, 012089. [CrossRef]
23. Jaya, N.A.; Liew, Y.M.; Heah, C.Y.; Abdullah, M.M.A.B.; Hussin, K. Correlation between pore structure, compressive strength and thermal conductivity of porous metakaolin geopolymer. *Constr. Build. Mater.* **2020**, *247*, 118641. [CrossRef]
24. Su, L.J.; Fu, G.S.; Li, F.Y.; Sun, Q.; Wang, J.L.; Zhang, J.N. Preparation and mechanical properties of coal gangue-based foamed geopolymer. *Bull. Chin. Ceram. Soc.* **2020**, *39*, 3549–3556. [CrossRef]
25. Gao, H.; Liu, H.; Liao, L.; Mei, L.; Zhang, F.; Zhang, L.; Li, S.; Lv, G. A bifunctional hierarchical porous kaolinite geopolymer with good performance in thermal and sound insulation. *Constr. Build. Mater.* **2020**, *251*, 118888. [CrossRef]
26. Berkouche, A.; Belkadi, A.A.; Noui, A.; Chiker, T.; Dridi, M.; Aggoun, S.; Douadi, A.; Chajec, A. Modeling and optimization of eco-friendly cellular foam geopolymer with recycled concrete and glass wastes using Box-Behnken design. *Structures* **2025**, *76*, 109054. [CrossRef]
27. Rong, X.; Zhang, X.; Zhang, J.; Xu, W.; Zhang, Z. Study on mechanical and thermal properties of alkali-excited fly ash aerogel foam concrete. *Constr. Build. Mater.* **2023**, *408*, 133770. [CrossRef]
28. Pan, P.; Yang, W.; Guo, Z. Improvement of thermal properties of foam concrete by incorporating silica aerogel particles. *Constr. Build. Mater.* **2025**, *478*, 141450. [CrossRef]

29. Ji, Y.; Sun, Q. The Stabilizing Effect of Carboxymethyl Cellulose on Foamed Concrete. *Int. J. Mol. Sci.* **2022**, *23*, 15473. [CrossRef] [PubMed]
30. Pessina, S. The Link Between Environmental Rights and the Rights of Nature: The Virtues of a Complexity-Based Approach. *Jurid. Trib.-Rev. Comp. Int. Law* **2025**, *15*, 406–422. [CrossRef]
31. *JGJ/T 341-2014*; Technical Specification for Application of Foamed Concrete. China Architecture and Building Press: Beijing, China, 2014.
32. *JGJ/T 323-2014*; Technical Specification for Application of Self-Insulation Concrete Compound Block Walls. China Architecture and Building Press: Beijing, China, 2014.
33. *GB 50574-2010*; Technical Specification for Unified Application of Wall Materials. China Architecture & Building Press: Beijing, China, 2011.
34. Jiangsu Provincial Department of Housing and Urban-Rural Development. *Technical Guidelines for Ultra-Low Energy Residential Buildings (Trial Implementation)*; Jiangsu Provincial Department of Housing and Urban-Rural Development: Nanjing, China, 2020.
35. Shanghai Municipal Housing and Urban-Rural Development Administration. *Technical Guidelines for Ultra-Low Energy Buildings (Trial Implementation)*; Shanghai Municipal Housing and Urban-Rural Development Administration: Shanghai, China, 2019.
36. *GB/T 51350-2019*; Technical Standard for Nearly Zero Energy Buildings. China Architecture and Building Press: Beijing, China, 2019.
37. *GB 50176-2016*; Code for Thermal Design of Civil Buildings. China Architecture and Building Press: Beijing, China, 2017.
38. *JC/T 2199-2013*; Foaming Agent for Foamed Concrete. China Building Materials Industry Press: Beijing, China, 2013.
39. Ye, T.; Xiao, J.; Duan, Z.; Li, S. Geopolymers made of recycled brick and concrete powder-A critical review. *Constr. Build. Mater.* **2022**, *330*, 127232. [CrossRef]
40. Alnahhal, A.M.; Alengaram, U.J.; Yusoff, S.; Darvish, P.; Srinivas, K.; Sumesh, M. Engineering performance of sustainable geopolymer foamed and non-foamed concretes. *Constr. Build. Mater.* **2022**, *316*, 125601. [CrossRef]
41. Gu, G.; Xu, F.; Huang, X.; Ruan, S.; Peng, C.; Lin, J. Foamed geopolymer: The relationship between rheological properties of geopolymer paste and pore-formation mechanism. *J. Clean. Prod.* **2020**, *277*, 123238. [CrossRef]
42. Ryu, G.S.; Lee, Y.B.; Koh, K.T.; Chung, Y.S. The mechanical properties of fly ash-based geopolymer concrete with alkaline activators. *Constr. Build. Mater.* **2013**, *47*, 409–418. [CrossRef]
43. Bodur, B.; Bayraktar, O.Y.; Benli, A.; Kaplan, G.; Tobbala, D.E.; Tayeh, B. Effect of using wastewater from the ready-mixed concrete plant on the performance of one-part alkali-activated GBFS/FA composites: Fresh, mechanical and durability properties. *J. Build. Eng.* **2023**, *76*, 107167. [CrossRef]
44. John, S.K.; Nadir, Y.; Girija, K. Effect of source materials, additives on the mechanical properties and durability of fly ash and fly ash-slag geopolymer mortar: A review. *Constr. Build. Mater.* **2021**, *280*, 122443. [CrossRef]
45. Wagh, C.D.; Gandhi, I.S.R. Investigations on the performance of xanthan gum as a foam stabilizer and assessment of economic and environmental impacts of foam concrete production. *J. Build. Eng.* **2024**, *82*, 108286. [CrossRef]
46. Bayraktar, O.Y.; Kaplan, G.; Gencel, O.; Benli, A.; Sutcu, M. Physico-mechanical, durability and thermal properties of basalt fiber reinforced foamed concrete containing waste marble powder and slag. *Constr. Build. Mater.* **2021**, *288*, 123128. [CrossRef]
47. Hwang, C.-L.; Yehualaw, M.D.; Vo, D.-H.; Huynh, T.-P.; Largo, A. Performance evaluation of alkali activated mortar containing high volume of waste brick powder blended with ground granulated blast furnace slag cured at ambient temperature. *Constr. Build. Mater.* **2019**, *223*, 657–667. [CrossRef]
48. Sheng, Y.; Peng, Y.; Zhang, S.; Guo, Y.; Ma, L.; Zhang, H. Thermal stability of foams stabilized by fluorocarbon and hydrocarbon surfactants in presence of nanoparticles with different specific surface areas. *J. Mol. Liq.* **2022**, *365*, 120187. [CrossRef]
49. Liu, X.; Wu, Y.; Li, M.; Jiang, J.; Guo, L.; Wang, W.; Zhang, W.; Zhang, Z.; Duan, P. Effects of graphene oxide on microstructure and mechanical properties of graphene oxide-geopolymer composites. *Constr. Build. Mater.* **2020**, *247*, 118544. [CrossRef]
50. Su, L.; Fu, G.; Liang, B.; Sun, Q.; Zhang, X.; Shen, Z. Working performance and microscopic mechanistic analyses of municipal solid waste incineration (MSWI) fly ash-based self-foaming filling materials. *Constr. Build. Mater.* **2022**, *361*, 129647. [CrossRef]
51. Pasupathy, K.; Ramakrishnan, S.; Sanjayan, J. Enhancing the mechanical and thermal properties of aerated geopolymer concrete using porous lightweight aggregates. *Constr. Build. Mater.* **2020**, *264*, 120713. [CrossRef]
52. Yu, P.; Kirkpatrick, R.J.; Poe, B.; McMillan, P.F.; Cong, X. Structure of calcium silicate hydrate (C-S-H): Near-, Mid-, and far-infrared spectroscopy. *J. Am. Ceram. Soc.* **2010**, *82*, 742–748. [CrossRef]

Disclaimer/Publisher's Note: The statements, opinions and data contained in all publications are solely those of the individual author(s) and contributor(s) and not of MDPI and/or the editor(s). MDPI and/or the editor(s) disclaim responsibility for any injury to people or property resulting from any ideas, methods, instructions or products referred to in the content.